People`s Democratic Republic of Algeria
Ministry of Higher Education and Scientific Research
University of Echahid Hamma Lakhdar - El Oued
Faculty of Technology
Department of Electrical Engineering

Dissertation
ACADEMIC MASTER
Domain: Science and Technology
Division: Telecommunication
Specialty: Telecommunication Systems

Presented by:
1. **Youcef Guenoua**

Entitled:

Design and simulation of high efficiency ultra-broadband solar energy absorber based on metasurface structure

Dissertation Submitted in Partial Fulfillment of the Requirements for the Master II Degree in communication systems

Publicly defended in: 28 /05 /2025

Board of Examiners:

Assistant professor. Abdellah Friteh	**Chairman**
Professor. Abdelkader Medjouri	**Supervisor**
Assistant professor. Imad Eddine Tinedert	**Examiner**

Academic Year: 2024/2025

ABSTRACT

We propose a novel metamaterial-based broadband solar absorber and thermal emitter for thermophotovoltaic (TPV) applications. The designed structure consists of two concentric cylinders placed atop a dielectric spacer, with a manganese (Mn) layer as the bottom reflector. The absorber leverages the synergistic effects of plasmonic and photonic resonances to achieve high absorption across a broad spectrum, maximizing solar energy harvesting. The manganese backing enhances absorption efficiency while ensuring high thermal stability and selective thermal emission in the infrared range, which is crucial for efficient TPV conversion. Finite-difference time-domain (FDTD) simulations confirm that the proposed structure exhibits near-unity absorption over a wide spectral range, making it a promising candidate for next-generation solar energy and thermophotovoltaic systems.

Key words: thermophotovoltaic systems, metamaterial absorber, solar energy harvesting, FDTD.

الملخص

نقترح ماصا شمسيا عريض النطاق ومصدرا حراريا قائما على المواد الفوقية الجديدة لتطبيقات أنظمة الطاقة الحرارية الضوئية (TPV). يتكون الهيكل المصمم من أسطوانتين متحدتي المركز موضوعتين أعلى فاصل عازل، مع طبقة منغنيز (Mn) كعاكس سفلي. يستفيد الماص من التأثيرات التآزرية للرنين البلازموني والفوتوني لتحقيق امتصاص عال عبر طيف واسع، مما يزيد من حصاد الطاقة الشمسية إلى أقصى حد. تعزز الطبقة الخلفية من المنغنيز كفاءة الامتصاص مع ضمان استقرار حراري عال وانبعاث حراري انتقائي في النطاق تحت الأحمر، وهو أمر حاسم لتحويل الطاقة الحرارية الضوئية بكفاءة. تؤكد محاكاة الفرق المحدود في المجال الزمني (FDTD) أن الهيكل المقترح يظهر امتصاصا شبه كامل عبر نطاق طيفي واسع، مما يجعله مرشحا واعدا لأنظمة الطاقة الشمسية وأنظمة الطاقة الحرارية الضوئية من الجيل التالي.

الكلمات المفتاحية: أنظمة الطاقة الحرارية الضوئية، ماص المواد الفوقية، حصاد الطاقة الشمسية، محاكاة الفرق المحدود في المجال الزمني (FDTD).

DEDICATION

To those who were the light that illuminated my path and the support that strengthened my resolve, I dedicate this humble work:

To my honorable parents, who instilled in my heart the values of knowledge and patience, and nurtured me with their boundless love and sincere prayers, forming the cornerstone of my journey.

To my beloved wife, my companion on this path and partner in dreams, who has been my support and inspiration with her patience and optimism.

To my dear children, you are the joy of my life and my motivation to strive for the best; this achievement is part of my hope to build a future worthy of you.

To my loyal siblings, who shared with me moments of joy and challenge, standing as an unwavering support.

To my esteemed colleagues and professors, who enlightened my mind with their knowledge and supported it with their valuable guidance.

And to everyone who contributed with a word of encouragement, a sincere prayer, or a hidden effort, you are partners in this achievement.

My heartfelt thanks to you all, praying to Almighty God to reward you with the best, and that this work be sincere for His noble sake and beneficial to knowledge and humanity.

THANKS, AND APPRECIATION

Praise be to Allah, Lord of the worlds, who has guided and enabled me, and granted me the blessing of knowledge and intellect. To Him belong abundant gratitude and everlasting praise for His favors and grace.

I extend my heartfelt thanks and gratitude to my esteemed professor, Pr. Abdelkader Medjouri, the supervisor of this work, who, after Allah, played the greatest role in the completion of this achievement. He illuminated the path of research with his vast expertise and profound knowledge of the subject, and his commendable humility, dedication to giving, and commitment to precise guidance accelerated the pace of this work’s completion, while his mutual respect added profound human and scientific value to the experience.

I also express my deep appreciation and gratitude to every professor who imparted knowledge or an idea that enriched this work. Their lessons and guidance throughout the stages of study served as the building blocks that contributed to shaping this research.

I offer special thanks to the distinguished members of the examination committee, chair, supervisor, and examiners, for the time and effort they dedicated to evaluating this work and enriching it with their valuable insights.

I pray to Almighty Allah to reward everyone with the best of rewards, and that this work be sincere for His noble sake and contribute to the service of knowledge and society.

TABLE OF CONTENTS

LIST OF FIGURES

LIST OF TABLES

LIST OF ABBREVIATIONS

TPV	thermophotovoltaic
Mn	manganese
FDTD	Finite-difference time-domain
EMWs	electromagnetic waves
MMs	metamaterials
EM	electromagnetic
MMAs	metamaterial absorbers
EMI	electromagnetic interference
MIM	metal-insulator-metal
$\mathbf{Al_2O_3}$	aluminum oxide
OMMs	optical metamaterials
RCS	radar cross-section
STPV	solar thermophotovoltaic
$\boldsymbol{A_{aver}}$	average absorption rate
SPR	surface plasmon resonance
CR	cavity resonance
MR	magnetic resonance

INTRODUCTION

The absorption of electromagnetic waves (EMWs) in the optical and terahertz domains is considered one of the leading topics in modern research fields, where metamaterials (MMs) emerge as a revolutionary tool for designing highly efficient absorbers. These materials are distinguished by their unique electromagnetic (EM) properties resulting from their precise subwavelength design, enabling precise control over their interaction with EMWs [15]. This thesis aims to explore the design and analysis of metamaterial absorbers (MMAs) in the optical and terahertz ranges, with a focus on their applications in solar energy absorption, as it is an area of increasing interest targeted by governments worldwide [16].

The significance of this research lies in the ability of MMAs to achieve near-perfect wave absorption across wide frequency ranges, opening new horizons in applications such as improving the efficiency of converting solar energy into heat or electricity [8], and enhancing the performance of communication systems by reducing electromagnetic interference (EMI) [9]. Moreover, the use of these absorbers lies in improving the performance of devices such as sensors and high-frequency wireless communication systems, contributing to the development of next-generation technologies [6].

The selection of this topic was driven by the growing need for innovative solutions to meet the requirements of modern communication systems and renewable energy applications [16]. MMs represent a promising field that combines applied physics and engineering, providing opportunities to develop advanced technologies that address global challenges in the fields of energy and communications. Furthermore, recent advancements in the design of broadband absorbers, such as those based on metal-insulator-metal (MIM) structures, have stimulated interest in studying these technologies for practical applications [13].

This research aims to provide a theoretical and practical analysis of MMAs, focusing on the design of a three-layer structure based on Mn cylinders and an aluminum oxide (Al_2O_3) dielectric layer. The research also seeks to study absorption mechanisms using the FDTD method and analyze the distribution of EM fields to understand the relationship between microscopic properties and the overall EM response. Additionally, the research aims to evaluate the efficiency of the proposed design in achieving ultra-broadband absorption compared to previous models.

The structure of this thesis includes three main chapters: the first chapter focuses on the theoretical foundations of electromagnetism, explaining fundamental laws such as Maxwell’s equations and the interaction of waves with materials. The second chapter addresses MMs and their absorbers, focusing on the optical properties of metal-insulator structures and absorption mechanisms. Finally, the third chapter reviews the applications of MMAs in solar energy absorption, proposing a new design based on an MIM structure to achieve enhanced performance. Through these chapters, the thesis seeks to provide a scientific contribution that advances the development of cutting-edge technologies in the fields of communications and renewable energy.

CHAPTER I ELEMENTS OF ELECTROMAGNETICS

I.1 Introduction

Electromagnetism is considered one of the fundamental pillars in both physics and electrical engineering, as it focuses on the study of electric and magnetic fields, as well as how they behave and interact in various environments. This chapter aims to establish a solid theoretical foundation for understanding the core principles of electromagnetism by exploring the key laws and models that explain the origin of electromagnetic EM fields and their interactions with matter, starting with Coulomb’s law, and culminating in Maxwell’s equations, which are regarded as the cornerstone for describing EM phenomena [1].

In addition, the chapter examines how EM waves propagate through different media and discusses the phenomenon of reflection under normal incidence. These concepts help lay the groundwork for understanding techniques used to control EM waves, knowledge that is essential for studying metamaterial-based absorbers.

I.2 Elements of electrostatics and magnetostatics (Time-invariant fields)

This section focuses on static fields. Stationary electric charges generate electric fields that do not vary with time, commonly referred to as electrostatics. On the other hand, steady currents produce constant magnetic fields, a phenomenon known as magnetostatics.

I.2.1 Electrostatics

The electrostatic field arises from the distribution of stationary electric charges, and its theoretical framework developed gradually over time. In 1785, Charles-Augustin de Coulomb formulated Coulomb’s law, which described the interaction between charges. Later, Carl Friedrich Gauss expanded the theoretical foundation by introducing Gauss’s law, establishing a core basis for studying electrostatic fields. Other scientists also contributed significantly to the field by presenting important findings related to the behavior of static charges [1].

I.2.1.1 Coulomb’s law and field intensity

Coulomb’s law describes the mutual force between two-point charges. It states that the force acts along the line connecting the charges, is directly proportional to the product of their magnitudes, and inversely proportional to the square of the distance between them.

The electric field intensity, also referred to as the electric field strength, represents the force experienced by a single positive test charge placed in the field. It is measured in newtons per coulomb (N/C) or volts per meter (V/m) [2].

I.2.1.2 Electric fields due to continuous charge distributions

Point charges, at their core, are charges concentrated in an extremely small region of space. However, electric charge isn't limited to this form alone, it can also be distributed continuously along a line, across a surface, or throughout a volume. The electric field intensity resulting from such distributions can be seen as the sum of the fields produced by the many point charges that make up the overall distribution [3].

$$dQ = \rho_v dv \rightarrow Q = \int_v \rho_v dv \tag{I.1}$$

I.2.1.3 Electric flux density

The electric flux generated by the electric field $\vec{E}$ can be determined using the general definition of flux. The electric field intensity depends on the nature of the medium in which the charge is present. By defining a new vector field $\vec{D}$ according to the relation:

$$\vec{D} = \varepsilon_0 \vec{E} \tag{I.2}$$

The electric flux ψ can be expressed in terms of $\vec{D}$ as follows:

$$\psi = \int_S \vec{D} \cdot \overrightarrow{dS} \tag{I.3}$$

The constant ε_0 is known as the permittivity of free space (in farads per meter) and has the value

$$\varepsilon_0 = 8.854 \times 10^{-12} \cong \frac{10^{-9}}{36\pi} (F/m) \tag{I.4}$$

Electric flux is measured in coulombs, and the vector field $\vec{D}$ is known as the electric flux density, measured in coulombs per square meter (C/m^2) [1].

I.2.1.4 Gauss's law - Maxwell's equation

Gauss's law states that the total electric flux ψ through any closed surface is equal to the total charge enclosed by that surface: $\psi = Q_{enc}$ .That is:

$$\psi = \oint_S \vec{D} \cdot \overrightarrow{dS} = Q_{enc} \Longrightarrow \oint_S \vec{E} \cdot \overrightarrow{dS} = \frac{Q_{enc}}{\varepsilon_0} \tag{I.5}$$

This is the integral form of the Gauss's law.

$$\oint_S \vec{D} \cdot \overrightarrow{dS} = Q_{enc} = \int_v \rho_v dv \tag{I.6}$$

By applying divergence theorem

$$\oint_S \vec{D} \cdot \overrightarrow{dS} = \int_v \vec{\nabla} \cdot \vec{D} dv \tag{I.7}$$

Comparing the two volume integrals results in:

$$\vec{\nabla} \cdot \vec{D} = \rho_v \Longrightarrow \vec{\nabla} \cdot \vec{E} = \frac{\rho_v}{\varepsilon_0} \tag{I.8}$$

This is the differential or point form of the Gauss's law [2].

I.2.1.5 Electric potential

Assume moving a point charge Q from point A to point B in an electric field $\vec{E}$, the work done in moving it by dl is:

$$dW = -Q\vec{E} \cdot \overrightarrow{dl} \tag{I.9}$$

The total work done is:

$$W = -Q \int_A^B \vec{E} \cdot \overrightarrow{dl} \tag{I.10}$$

When W is divided by Q, we obtain the potential energy per unit charge, denoted as V_{AB} , which is known as the electric potential difference between points A and B [4], therefore:

$$V_{AB} = \frac{W}{Q} = -Q \int_A^B \vec{E} \cdot \overrightarrow{dl} \tag{I.11}$$

Given that $V_{AB} = -V_{BA}$, hence:

$$V_{AB} + V_{BA} = \oint_L \vec{E} \cdot \overrightarrow{dl} = 0 \tag{I.12}$$

Applying Stokes's theorem gives:

$$\oint_L \vec{E} \cdot \overrightarrow{dl} = \int_S \left(\vec{\nabla} \times \vec{E}\right) \cdot \overrightarrow{dS} = 0 \text{ , or } \vec{\nabla} \times \vec{E} = 0 \tag{I.13}$$

Thus, an electrostatic field is a conservative (irrotational) field [3].

I.2.2 Magnetostatics

Magnetostatic fields are governed by two fundamental laws: the first is Biot-Savart's law, which serves as the general principle in magnetostatics, and the second is Ampère's circuital law, considered a special case of the former. This relationship is similar to what we see in electrostatics, where Gauss's law is essentially a specific application of Coulomb's law. One of the advantages of Ampère's law is its ease of use in solving problems involving symmetric current distributions.

I.2.2.1 Biot-Savart's law

Biot-Savart's law states that the differential magnetic field intensity dH produced at a point *P*, by the differential current element $I\ dl$ is proportional to the product $I\ \overrightarrow{dl}$ and the sine of the angle α between the element and the line joining P to the element and is inversely proportional to the square of the distance *R* between *P* and the element [2].

I.2.2.2 Ampère's circuit law - Maxwell's equation

Ampère's circuit law states that the line integral of $\vec{H}$ around a closed path is the same as the net current I_{enc} enclosed by the path. In other words, the circulation of $\vec{H}$ equals I_{enc}:

$$\oint_L \vec{H} \cdot \overrightarrow{dl} = I_{enc} \tag{I.14}$$

By applying Stokes's theorem:

$$\oint_L \vec{H} \cdot \overrightarrow{dl} = \int_S \left(\vec{\nabla} \times \vec{H}\right) \cdot \overrightarrow{dS} \tag{I.15}$$

We define $\vec{J}$ as the volume current density in amperes per meter squared (A/m^2) [1]. But

$$I_{enc} = \int_S \vec{J} \cdot \overrightarrow{dS} \Rightarrow \vec{\nabla} \times \vec{H} = \vec{J} \tag{I.16}$$

I.2.2.3 Magnetic flux density - Maxwell's equation

The magnetic flux density $\vec{B}$ is analogous to its electric counterpart the electric flux density $\vec{D}$. in free space the magnetic flux density $\vec{B}$ is related to the magnetic field intensity $\vec{H}$ by the equation:

$$\vec{B} = \mu_0 \vec{H} \tag{I.17}$$

$$\mu_0 = 4\pi \times 10^{-7} (H/m) \tag{I.18}$$

Where μ_0 represents the permeability of free space [2].

The magnetic flux through a surface S is given by:

$$\psi = \int_S \vec{B} \cdot \overrightarrow{dS} \tag{I.19}$$

Where the magnetic flux ψ is in webers (Wb) and the magnetic flux density $\vec{B}$ is in Weber's per square meter (Wb/m^2) or teslas (T) [3].

A magnetic flux line is a path along which $\vec{B}$ is tangential at every point on the line. Regardless of the current distribution, magnetic flux lines are always closed upon themselves and do not intersect. Consequently, the total flux through any closed surface within a M field must be zero.

$$\oint_S \vec{B} \cdot \overrightarrow{dS} = 0 \tag{I.20}$$

This equation is known as the law of conservation of magnetic flux or Gauss's law for magnetostatic fields. By applying the divergence theorem [1], we obtain:

$$\oint_S \vec{B} \cdot \overrightarrow{dS} = \int_v \vec{\nabla} \cdot \vec{B}\, dv = 0 \text{ or } \vec{\nabla} \cdot \vec{B} = 0 \tag{I.21}$$

I.3 Time-Varying Fields and Maxwell's Equations

In the previous section, we explored the basic relationships governing electrostatic and magnetostatic fields. We now turn our attention to time-varying fields. This section focuses on two essential concepts: the generation of an electric field caused by a changing magnetic field, which was discovered experimentally by Faraday, and the creation of a magnetic field resulting from a changing electric field, which was theoretically established by Maxwell [2].

I.3.1 Faraday's law

In 1831, both Michael Faraday in London and Joseph Henry in New York discovered that a time-varying magnetic field could generate an electric current. According to Faraday's experiments, a static magnetic field does not produce any current, but in a closed circuit, a time-varying field induces a voltage (known as electromotive force or emf), which leads to the flow of electric current [1].

Faraday discovered that the induced emf, V_{emf} (in volts) in any closed circuit is equal to the time rate of change of the magnetic flux linkage by the circuit, this is called Faraday's law, and it can be expressed as:

$$V_{emf} = -N\frac{d\psi}{dt} \qquad (I.22)$$

N is the number of turns in the circuit, and is the flux through each turn. The negative sign shows that the induced voltage acts in such a way as to oppose the flux producing it. This behaviour is described as Lenz's law. For a circuit with a single turn ($N = 1$), Faraday's law becomes:

$$V_{emf} = \oint_L \vec{E}\cdot\overrightarrow{dl} = -\frac{d}{dt}\int_S \vec{B}\cdot\overrightarrow{dS} \qquad (I.23)$$

By applying Stokes's theorem, we obtain:

$$\oint_L \vec{E}\cdot\overrightarrow{dl} = \int_S \left(\vec{\nabla}\times\vec{E}\right)\cdot\overrightarrow{dS} = -\frac{d}{dt}\int_S \vec{B}\cdot\overrightarrow{dS} \qquad (I.24)$$

For the two integrals to be equal, their integrands must be equal, that is:

$$\vec{\nabla}\times\vec{E} = -\frac{\partial\vec{B}}{\partial t} \qquad (I.25)$$

This is one of the Maxwell's equations for time-varying fields. It shows that the time-varying $\vec{E}$ field is not conservative $\left(\vec{\nabla}\times\vec{E}\right) \neq 0$ [1].

I.3.2 Displacement current, (the Ampere–Maxwell law)

Ampere's law, which links steady electric current to the magnetic field, had already been established before Maxwell began his work in the 1850s. However, it was limited to static scenarios. Maxwell expanded on this by introducing the idea that a changing electric flux could also act as a source, allowing the law to apply to time-varying situations. This key insight paved the way for understanding light as an EM wave and laid the foundation for a unified theory of electromagnetism. The need for this addition becomes clear when examining the inconsistency in Ampere's law in the case of a charging capacitor [2].

In the circuit illustrated below (Figure I.1), closing the switch initiates a current I that charges the capacitor and creates a magnetic field around the connecting wires, as described by Ampère's law:

$$\oint_L \vec{B}\cdot\overrightarrow{dl} = \mu_0 I \qquad (I.26)$$

The challenge lies in identifying the current enclosed by the loop, which should account for all currents passing through any surface bounded by path C. If we choose a flat surface that intersects the wire, the current I clearly passes through it. However, if we instead use a domed surface, like a "stocking cap", spanning the space between the capacitor plates, no conduction current passes through, since charges accumulate on the plates without crossing the gap. Still, because both surfaces share the same boundary loop, the line integral of the magnetic field must yield the same result. This implies the existence of an additional source contributing to the magnetic field. That missing element is known as the displacement current, not a real current of moving charges, but a term that arises due to the changing electric field between the capacitor plates [4].

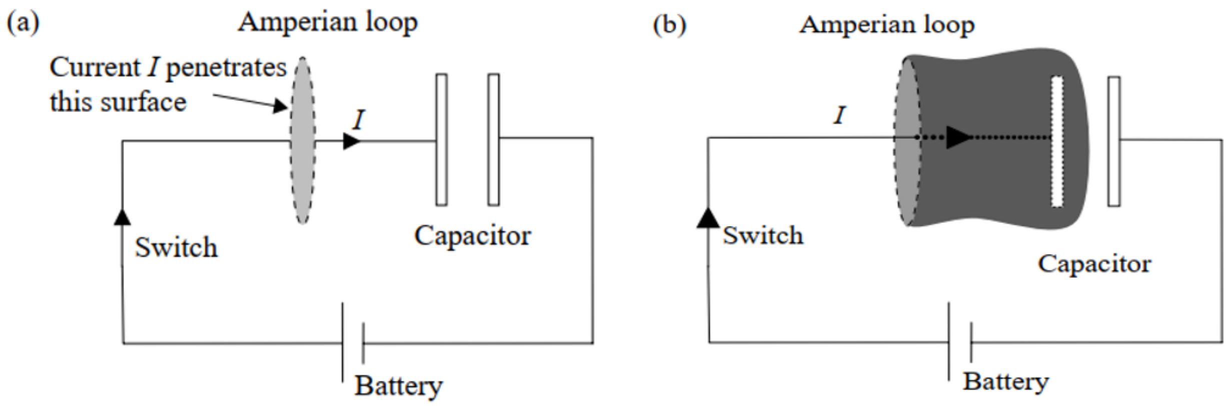

Figure I.1 Alternative surfaces for determining enclosed current [4].

The displacement current is defined by the relation:

$$I_d = \varepsilon_0 \frac{d}{dt} \oint_S \vec{E} \cdot \overrightarrow{dS} \tag{I.27}$$

Maxwell's equation (based on Ampere's circuit law) for a time-varying field is given by:

$$\oint_L \vec{B} \cdot \overrightarrow{dl} = \mu_0 \left(I + \varepsilon_0 \frac{d}{dt} \int_S \vec{E} \cdot \overrightarrow{dS} \right) = \mu_0 \left(\int_S \vec{J} \cdot \overrightarrow{dS} + \varepsilon_0 \frac{d}{dt} \int_S \vec{E} \cdot \overrightarrow{dS} \right) \tag{I.28}$$

And applying Stokes' theorem:

$$\vec{\nabla} \times \vec{B} = \mu_0 \left(\vec{J} + \varepsilon_0 \frac{d}{dt} \vec{E} \right) \tag{I.29}$$

The displacement current density:

$$\vec{J}_d = \varepsilon_0 \frac{d}{dt} \vec{E} \tag{I.30}$$

The conduction current density $\vec{J} = \vec{J}_d = \sigma \vec{E}$, (σ is the conductivity) [3].

I.3.3 Maxwell's equations in final forms

James Clerk Maxwell (1831-1879) is regarded as the founding figure of modern EM theory, as his research led to the discovery of EM waves. Between the ages of 35 and 40, he developed the first unified theory of electricity and magnetism, building upon earlier findings and introducing the concept of displacement current, through which he predicted the existence of EM waves. His equations did not gain widespread recognition until 1888, when Heinrich Hertz experimentally validated them by generating and detecting radio waves [1].

Maxwell's electromagnetic laws are expressed through four equations, shown in the table below. The divergence equations remained unchanged, while the curl equations were modified. The integral form of these equations represents fundamental physical laws, whereas the differential form is commonly used to solve practical problems. For a field to be classified as electromagnetic, it must satisfy all of Maxwell's equations, which collectively summarize all known principles of electromagnetism [2].

Table I.1 Maxwell's Four Equations governing EM fields [1]

Generalized Forms of Maxwell's Equations		
Integral Form	Differential Form	Remarks
$\oint_S \vec{E}\cdot\overrightarrow{dS}=\frac{Q_{enc}}{\varepsilon_0}$	$\vec{\nabla}\cdot\vec{E}=\frac{\rho_v}{\varepsilon_0}$	Gauss's law
$\oint_S \vec{B}\cdot\overrightarrow{dS}=0$	$\vec{\nabla}\cdot\vec{B}=0$	Nonexistence of isolated magnetic charge
$\oint_L \vec{E}\cdot\overrightarrow{dl}=-\frac{d}{dt}\int_S \vec{B}\cdot\overrightarrow{dS}$	$\vec{\nabla}\times\vec{E}=-\frac{\partial\vec{B}}{\partial t}$	Faraday's law
$\oint_L \vec{B}\cdot\overrightarrow{dl}=\mu_0\left(\int_S \vec{J}\cdot\overrightarrow{dS}+\varepsilon_0\frac{d}{dt}\int_S \vec{E}\cdot\overrightarrow{dS}\right)$	$\vec{\nabla}\times\vec{B}=\mu_0\left(\vec{J}+\varepsilon_0\frac{d}{dt}\vec{E}\right)$	Ampere's circuit law

I.3.4 From Maxwell's Equations to the wave equation

By applying the differential form of Maxwell's equations along with some vector calculus identities, we can derive the wave equation quite straightforwardly [4]. The process begins by taking the curl of both sides of Faraday's law in its differential form:

$$\vec{\nabla}\times\left(\vec{\nabla}\times\vec{E}\right)=\vec{\nabla}\times\left(-\frac{\partial\vec{B}}{\partial t}\right)=-\frac{\partial\left(\vec{\nabla}\times\vec{B}\right)}{\partial t} \tag{I.31}$$

$$\vec{\nabla}\times\left(\vec{\nabla}\times\vec{E}\right)=\vec{\nabla}\left(\vec{\nabla}\cdot\vec{E}\right)-\Delta\vec{E}=-\frac{\partial\left(\mu_0\left(\vec{J}+\varepsilon_0\frac{d}{dt}\vec{E}\right)\right)}{\partial t} \tag{I.32}$$

$$\vec{\nabla}\times\left(\vec{\nabla}\times\vec{E}\right)=\vec{\nabla}\left(\frac{\rho_v}{\varepsilon_0}\right)-\Delta\vec{E}=-\mu_0\frac{d\vec{J}}{dt}-\mu_0\varepsilon_0\frac{d^2\vec{E}}{dt^2} \tag{I.33}$$

$$\Delta\vec{E}-\mu_0\varepsilon_0\frac{d^2\vec{E}}{dt^2}=\vec{\nabla}\left(\frac{\rho_v}{\varepsilon_0}\right)+\mu_0\frac{d\vec{J}}{dt} \tag{I.34}$$

In a charge- and current-free region, $\rho_v=0, \vec{J}=0$. So:

$$\Delta\vec{E}-\mu_0\varepsilon_0\frac{d^2\vec{E}}{dt^2}=0 \tag{I.35}$$

A similar analysis beginning with the curl of both sides of the Ampere-Maxwell law leads to:

$$\Delta\vec{B}-\mu_0\varepsilon_0\frac{d^2\vec{B}}{dt^2}=0 \tag{I.36}$$

This is a second-order linear partial differential equation that characterizes how the electric or magnetic field propagates as a wave, and also defines its speed:

$$\frac{1}{v^2}=\mu_0\varepsilon_0 \longrightarrow v=\sqrt{\frac{1}{\mu_0\varepsilon_0}}=2.9979\times10^8(m/s) \tag{I.37}$$

It was the fact that the calculated propagation velocity matched the measured speed of light that led Maxwell to conclude, "light is an electromagnetic disturbance that travels through the field in accordance with electromagnetic laws" [1].

I.4 Electromagnetic waves propagation

Heinrich Hertz confirmed the existence of EM waves, which were predicted by Maxwell's equations, by successfully generating and detecting radio waves, often referred to as "Hertzian waves." In general, waves are used to carry energy or information, like radio waves, television signals, radar beams, and light rays [2].

I.4.1 Waves in general

A wave depends on both space and time, as it propagates when a disturbance at point A at a given time is related to what happens at point B at a later time. The wave equation is a second-order partial differential equation, and in one dimension, it takes the following form:

$$\frac{d^2E}{dt^2} - u^2\frac{d^2E}{dz^2} = 0 \tag{I.38}$$

Here, u represents the speed at which the wave travels [1].

If we particularly assume harmonic (or sinusoidal) time dependence, the wave equation becomes:

$$\frac{d^2E_S}{dz^2} + \beta^2 E_S = 0 \tag{I.39}$$

Where $\beta = \omega/u$. For now, let us consider the solution to the wave equation:

$$E = A\sin(\omega t - \beta z) \tag{I.40}$$

A wave repeats itself after traveling a certain distance, known as the wavelength (in meters). The time it takes for this repetition is T, referred to as the period (in seconds). Since the wave travels a distance λ lambda at a speed u within the time T, this can be expressed by the equation: $\lambda = uT$ or $u = \lambda/T = \lambda f$. Also, because: $\omega = 2\pi f$ and $\beta = \omega/u$, we expect: $\beta = 2\pi/\lambda$ [2].

I.4.2 Wave propagation in lossy dielectrics

The propagation of waves in lossy dielectrics represents the general case from which wave propagation in other media can be derived as special cases [1]. In this medium, the EM wave loses energy as it propagates due to the imperfection of the dielectric, making it a partially conductive (non-ideal) medium, where $\sigma \neq 0$, unlike a perfect or good dielectric, where $\sigma = 0$.

Let us consider a linear, homogeneous, and charge-free lossy dielectric medium, where Maxwell's equations take the following form when the time dependence $e^{j\omega t}$ is neglected:

$$\vec{\nabla}\cdot\overrightarrow{E_S} = 0, \vec{\nabla}\cdot\overrightarrow{H_S} = 0, \vec{\nabla}\times\overrightarrow{E_S} = -j\omega\mu\overrightarrow{H_S}, \vec{\nabla}\times\overrightarrow{H_S} = (\sigma + j\omega\varepsilon)\overrightarrow{E_S} \tag{I.41}$$

γ in reciprocal meters, is called the propagation constant of the medium we may let $\gamma = \alpha + j\beta$ with:

$$\alpha = \omega\sqrt{\frac{\mu\varepsilon}{2}\left[\sqrt{1+\left(\frac{\sigma}{\omega\varepsilon}\right)^2}-1\right]}, \beta = \omega\sqrt{\frac{\mu\varepsilon}{2}\left[\sqrt{1+\left(\frac{\sigma}{\omega\varepsilon}\right)^2}+1\right]} \tag{I.42}$$

The solution to the wave equation is given by for both the electric and magnetic fields [1]:

$$\vec{E}(z,t) = E_0 e^{-\alpha z}\cos(\omega t - \beta z)\,\overrightarrow{u_x} \tag{I.43}$$

$$\vec{H}(z,t) = Re\left(H_0 e^{-\alpha z} e^{(\omega t-\beta z)}\overrightarrow{u_y}\right) \tag{I.44}$$

Where $H_0 = \frac{E_0}{\eta}$, η is a complex quantity known as the intrinsic impedance, in ohms, of the medium. It can be shown:

$$\eta = \sqrt{\frac{j\omega\mu}{\sigma + j\omega\varepsilon}} \tag{I.45}$$

As the wave propagates along the $\overrightarrow{u_z}$ direction, its amplitude gradually decreases by a factor of $e^{-\alpha z}$, therefore α is called the attenuation constant or attenuation coefficient, measured in nepers per meter (Np/m), and it can also be expressed in decibels per meter (dB/m), 1 Np = 8.686 dB [2].

I.4.3 Plane waves in lossless dielectrics

In a lossless dielectric, $\sigma \ll \omega\varepsilon$, in this case: $\sigma \cong 0, \varepsilon = \varepsilon_r\varepsilon_0, \mu = \mu_r\mu_0$, consequently $\alpha = 0, \beta = \omega\sqrt{\mu\varepsilon}, u = \frac{\omega}{\beta} = \frac{1}{\sqrt{\mu\varepsilon}}, \lambda = \frac{2\pi}{\beta}, \eta = \sqrt{\frac{\mu}{\varepsilon}}$, thus $\vec{E}$ and $\vec{H}$are in time phase with each other.

I.4.4 Plane waves in good conductors

A perfect, or good conductor, is one in which $\sigma \gg \omega\varepsilon$, so that $\frac{\sigma}{\omega\varepsilon} \gg 1$, that is $\sigma \approx \infty, \varepsilon = \varepsilon_0, \mu = \mu_r\mu_0$, consequently $\alpha = \beta = \sqrt{\frac{\omega\mu\sigma}{2}}, u = \frac{\omega}{\beta} = \sqrt{\frac{2\omega}{\mu\sigma}}, \lambda = \frac{2\pi}{\beta}, \eta = \sqrt{\frac{\omega\mu}{\sigma}}$ and $\theta_\eta = 45^0$.

$$\vec{E}(z,t) = E_0 e^{-\alpha z}\cos(\omega t - \beta z)\,\overrightarrow{u_x} \tag{I.46}$$

$$\vec{H} = \frac{E_0}{\sqrt{\frac{\omega\mu}{\sigma}}} e^{-\alpha z}\cos(\omega t - \beta z - 45^0)\,\overrightarrow{u_y} \tag{I.47}$$

When an electromagnetic wave $\vec{E}$ or $\vec{H}$ propagates in a conducting medium, its amplitude gradually decreases by the factor $e^{-\alpha z}$. The distance at which the amplitude drops to about 37% of its original value is called the skin depth or penetration depth, and it is given by $\delta = \frac{1}{\alpha}$. In good conductors, where $\alpha = \beta = \frac{1}{\delta}$, the electric field can be expressed as:

$$\vec{E}(z,t) = E_0 e^{-z/\delta}\cos(\omega t - z/\delta)\,\overrightarrow{u_x} \tag{I.48}$$

The phenomenon in which the field intensity rapidly decreases inside the conductor is known as the Skin Effect. It refers to the tendency of electric charges to migrate from the interior of the conductor toward its surface, resulting in increased resistance. The fields and associated currents are thus confined to a very thin surface layer known as the skin [1].

I.5 Reflection of EM plane waves

Previously, we considered uniform plane waves in an unbounded, homogeneous medium. When such a wave encounters a different medium, it splits into a reflected wave and a transmitted wave, with their proportions determined by the properties of the two media $(\varepsilon, \mu, \sigma)$ [2].

I.5.1 Reflection of a plane wave at normal incidence

Suppose that a plane wave propagating along the + z-direction is incident normally on the boundary z = 0, between medium1(z < 0) characterized by $\varepsilon_1, \mu_1, \sigma_1$, and medium 2 (z > 0) characterized by $\varepsilon_2, \mu_2, \sigma_2$, as shown in the figure below (Figure I.2).

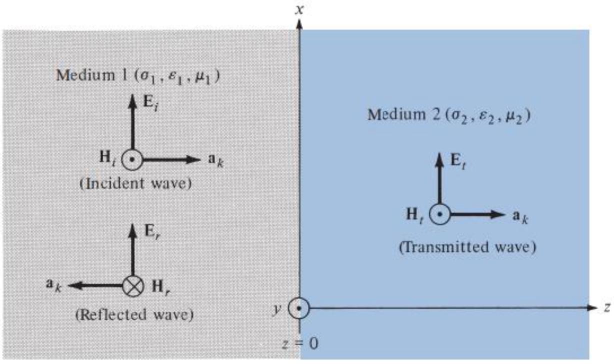

Figure I.2 A plane wave incident normally on an interface between two different media [1].

The symbols i, r, and t represent the incident, reflected, and transmitted waves, respectively. Each of these waves is defined as follows:

Incident wave: $\vec{E}_i, \vec{H}_i$ is traveling along $+\vec{u}_z$ in medium1

$$\vec{E}_{is}(z) = E_{i0} e^{-\gamma_1 z} \vec{u}_x \tag{I.49}$$

$$\vec{H}_{is}(z) = H_{i0} e^{-\gamma_1 z} \vec{u}_y = \frac{E_{i0}}{\eta_1} e^{-\gamma_1 z} \vec{u}_y \tag{I.50}$$

Reflected wave: $\vec{E}_r, \vec{H}_r$ is traveling along $-\vec{u}_z$ in medium1

$$\vec{E}_{rs}(z) = E_{r0} e^{\gamma_1 z} \vec{u}_x \tag{I.51}$$

$$\vec{H}_{rs}(z) = H_{r0} e^{\gamma_1 z} \left(-\vec{u}_y\right) = -\frac{E_{r0}}{\eta_1} e^{\gamma_1 z} \vec{u}_y \tag{I.52}$$

Transmitted wave: $\vec{E}_t, \vec{H}_t$ is traveling along $+\vec{u}_z$ in medium 2

$$\vec{E}_{ts}(z) = E_{t0} e^{-\gamma_2 z} \vec{u}_x \tag{I.53}$$

$$\vec{H}_{ts}(z) = H_{t0} e^{-\gamma_2 z} \vec{u}_y = \frac{E_{t0}}{\eta_2} e^{-\gamma_2 z} \vec{u}_y \tag{I.54}$$

We now define the reflection coefficient Γ and the transmission coefficient τ as:

$$\Gamma = \frac{E_{r0}}{E_{i0}} = \frac{\eta_2 - \eta_1}{\eta_2 + \eta_1}, \ \tau = \frac{E_{t0}}{E_{i0}} = \frac{2\eta_2}{\eta_2 + \eta_1} \tag{I.55}$$

In the special case where the first medium is a perfect dielectric (lossless) and the second is a perfect conductor (with infinite conductivity), the incident wave is completely reflected at the interface. This means the reflection coefficient $\Gamma = -1$ and the transmission coefficient $\tau = 0$, indicating that no transmitted wave exists within the conductor, as the electromagnetic fields vanish inside it. As a result, the incident wave combines with the reflected wave to form a standing wave, which does not propagate through the medium but instead oscillates both spatially and temporally [2].

I.6 Conclusion

In this chapter, we explored the theoretical foundations of EM radiation, beginning with the fundamental concepts of electricity and magnetism in both static and time-varying conditions. We then moved on to Maxwell's equations, which serve as a unified framework for understanding a wide range of EM phenomena. The chapter also covered the propagation of EM waves through various media, as well as the reflection of plane waves at interfaces, concepts that are essential for understanding how EM waves interact with materials.

These theoretical foundations provide the basis for understanding the operation of EM absorbers, particularly those based on metamaterials. Such structures rely heavily on phenomena like reflection, absorption, and wave propagation within precisely engineered geometries. In the following chapters, these principles will be applied to the analysis and design of metamaterial-based absorbers.

CHAPTER II METAMATERIAL ABSORBER

II.1 Introduction

As a novel class of engineered materials, metamaterials MMs exhibit unique EM properties arising from their precise subwavelength design, enabling unprecedented control over their interactions with EM fields. Among their diverse applications, metamaterial absorbers MMAs have emerged as one of the most extensively researched areas due to their exceptional efficiency in wave absorption across broad frequency ranges [5].

This chapter aims to provide a theoretical overview of the operational mechanisms of MMAs within the optical frequency range. It begins with the fundamental concepts of MMs and their historical development, then progresses to analyze characterization methodologies using effective models. The chapter also examines the optical behavior of metal-dielectric composites, highlighting the relationship between microscopic properties and macroscopic EM responses.

II.2 Metamaterials

Electromagnetic phenomena and devices fundamentally depend on how waves interact with materials. Engineers control these interactions by carefully designing structures using existing materials, though they're always constrained by the material's inherent limitations. But here's where it gets interesting, we can overcome these physical barriers by engineering artificial materials called MMs. Unlike conventional materials crafted at molecular levels, we construct MMs as carefully designed composite structures with sub-wavelength dimensions. This clever approach lets us describe their EM behaviour using effective homogeneous parameters. Our research specifically zooms in on structures that demonstrate extraordinary optical properties, what we call optical metamaterials (OMMs) [5].

II.2.1 Concept and evolution

MMs represent a fascinating class of engineered structures that outperform conventional materials in remarkable ways. The name itself comes from the Greek "meta" (meaning "beyond"), reflecting their extraordinary capabilities. While the term gained traction around 2000 after scientists created a material with negative ε and μ at microwave frequencies (some cite 1999 as the true starting point), the field has since exploded, drawing experts from physics, optics, materials science, and engineering. Ironically, despite their popularity, there's still no consensus definition, while many describe MMs as having unnatural properties, nature itself offers surprising parallels, from the negative refraction in lobster eyes to photonic structures in butterfly wings [6].

What truly defines MMs is their architectural ingenuity, their properties emerge not from material composition, but from precisely designed sub-wavelength structures. When these structures are significantly smaller than the operating wavelength, we can model their EM behavior using effective parameters. This scale matters profoundly: as structures approach the wavelength size (like in photonic crystals), diffraction effects dominate. The beauty of MMs lies in their design freedom, no specific arrangement is mandated, allowing endless innovation to achieve unprecedented EM functionality [5].

II.2.2 The historical evolution of MMs

Surprisingly, MMs have been hiding in plain sight for centuries! Take the famous Roman Lycurgus Cup (see Figure II.1), its color-changing magic from ancient nanotechnology (gold nanoparticles) predates modern physics by millennia. Long before the term "metamaterials" entered textbooks, researchers were already exploring similar concepts, like twisted jute fibers in 1898 and microwave engineers tinkering with artificial dielectrics [5].

The field truly exploded thanks to visionary work like Veselago's theory on left-handed materials (proposing negative ε and μ), later proven experimentally by Smith, that eureka moment when theory met reality. And let's not forget Pendry's perfect lens breakthrough that rewrote the rules. Initially focused on negative refraction (n), the field rapidly expanded to engineer materials with once-impossible properties, giving us unprecedented EM control [5].

Optics researchers were quick to jump on this bandwagon, making OMMs one of today's hottest, and toughest, research frontiers. Sometimes called photonic MMs (same difference), OMMs have benefited massively from cutting-edge nanofabrication and simulation tools, enabling mind-bending light manipulation [5].

Current research is chasing optical magnetism, negative-n materials, super-resolution imaging, and yes, real-life invisibility cloaks. These materials are completely reinventing optical device design through precision EM engineering. Despite hurdles like dispersion and loss, scientists keep pushing boundaries in optical sensing, nano-antennas, and subwavelength imaging applications [6].

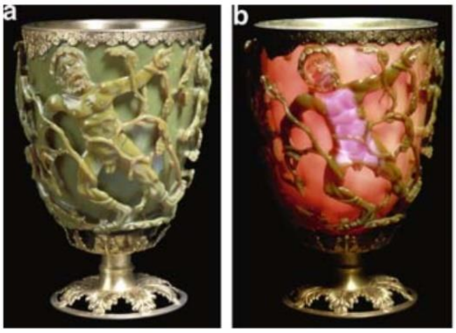

Figure II.1 The Lycurgus Cup viewed (a) in reflected light and (b) in transmitted light [5].

II.2.3 Types of MMs and properties

The study of artificial composite materials engineered to possess physical properties that surpass (or complement) those found in nature is the subject of an interdisciplinary research field known as MMs, which are frequently employed to modify the EM, acoustic, or elastic properties of materials. Figure II.2 presents a discussion on the various types of MMs and their properties.

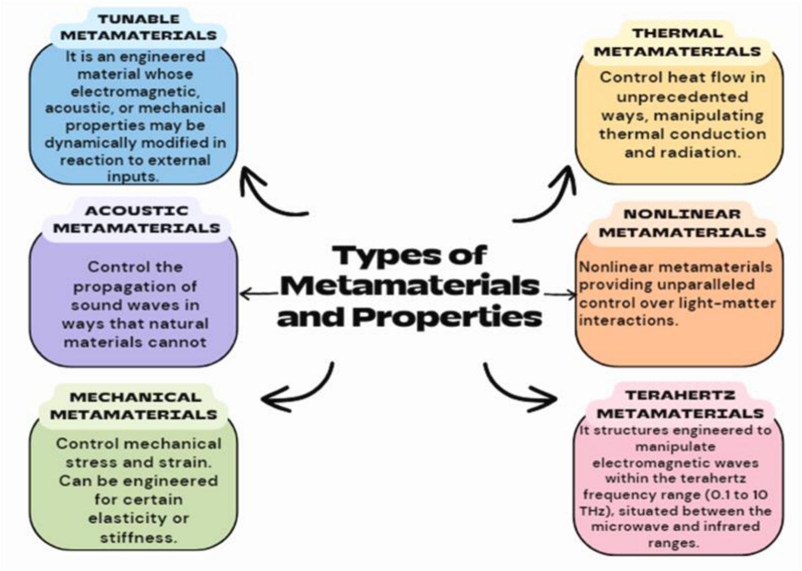

Figure II.2 Types of MMs and their properties [7].

II.3 Macroscopic effective parameters

At the heart of nearly all EM phenomena lie Maxwell's equations, those four elegant formulas that essentially explain how fields, charges, and materials interact. When EM waves hit a material, something fascinating happens: the electric fields make charges dance around while magnetic fields align tiny dipoles. What happens next depends entirely on the material's personality, some materials get electrically polarized (shifting their electron clouds), while others become magnetized (aligning their internal dipoles) [6].

II.3.1 Representation of EM properties in materials

Every material's EM personality comes down to four key parameters: its electric permittivity (ε), magnetic permeability (μ), refractive index ($n = \sqrt{\varepsilon\mu}$), and wave impedance ($Z = \sqrt{(\varepsilon/\mu)}$). These tell us how the material interacts with E and M fields. Zoom in to the microscopic level, and you'll see atoms arranged in orderly patterns, when light hits them, these atoms become tiny electric dipoles that create complex local field patterns. But here's the fascinating part: light itself doesn't "see" this intricate atomic dance or the absorption, radiation, processes happening at this scale. Why? Because Maxwell's equations smooth everything out at the macroscopic level [5].

At optical frequencies, we observe these interactions through measurable effects like reflection, transmission, time delays, and energy absorption. MMs play a clever trick, their internal structures are engineered to be so much smaller than the wavelength that, macroscopically, they appear perfectly uniform despite their complex nano-architecture. Just like conventional materials, we can describe their behavior using effective ε, μ, n, and Z values. The real magic happens in their carefully designed "meta-atoms", typically intricate metal-dielectric structures, that give us unprecedented control over EM responses [6].

II.3.2 Exploiting the EM parameter space

A material's reaction to EM fields boils down to its ε and μ values, creating what we might call an EM fingerprint that places each material in parameter space. Picture this: we plot ε_{r} on the x-axis and μ_{r} on the y-axis (see Figure II.3). Your everyday transparent materials cluster in quadrant I where both values stay positive, while negative values flip the script, literally reversing induced field directions. Gold and silver pull this trick at optical frequencies (negative-ε), while certain magnetic materials go negative near resonance (negative-μ) [5].

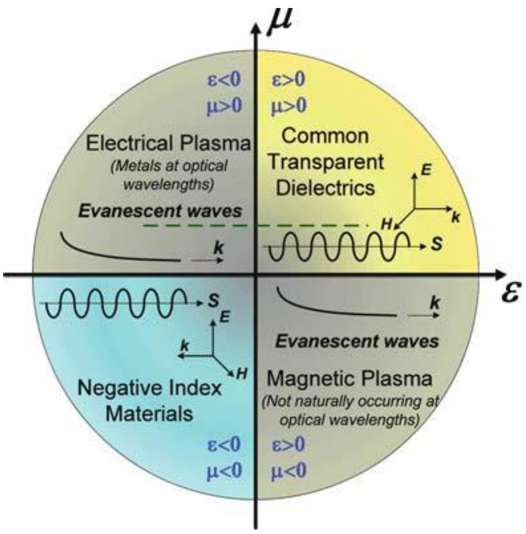

Figure II.3 The parameter space of permittivity ε and permeability μ [5].

Here's the catch: quadrants II and IV? Wave propagation gets blocked there because n turns imaginary. Most conventional optical materials hug the $\mu = 1$ line so tightly (dotted line in Figure II.3) they barely register. But MMs? They're rewriting the rulebook by exploring uncharted territory in this parameter space. Recent breakthroughs in optical magnetism finally cracked quadrant III with negative-n materials. As nanofabrication and computational methods keep advancing, we're not just mapping this space, we're learning to terraform it, opening radical new ways to sculpt light itself [5].

II.4 Optical properties of metal-dielectric composites

MMs are engineered structures composed of periodic units known as meta-atoms, whose composite architecture grants them unique properties distinct from their conventional components. This is analogous to cooking, where the final taste surpasses the sum of individual flavors. Similarly, designing OMMs requires an understanding of the properties of dielectrics, semiconductors, and metals, along with the study of the mechanisms governing their optical behavior, which this section aims to elucidate [5].

II.4.1 Optical materials and electronic structures

The classification of materials into insulators and metals in optics stems from electronic principles, where material properties are determined by electrical resistance. Insulators possess an energy band gap that prevents current flow, while metals contain free electrons that move easily under applied voltage, making them efficient conductors. Semiconductors, with their moderate band gap, enable controlled electron flow [6].

When examining optical properties, electronic structure must be considered. Insulators remain transparent to visible light because photon energy cannot bridge their band gap. However, electronic classification alone can be misleading, as demonstrated by indium tin oxide (ITO), electrically conductive yet optically transparent. Similar behavior occurs in metals like tungsten. In OMMs, semiconductors are often treated as insulators, being either transparent or absorbing depending on wavelength [5].

The crucial distinction between semiconductors and conventional insulators lies in band gap width. In electronics, narrow gaps enable precise electron control, driving semiconductor technology advancements. For optics, electron excitation depends on photon energy relative to the band gap $\mathrm{E_g}$, determining the critical transparency wavelength λ_c:

$$\lambda_\mathrm{c} = \frac{\mathrm{hc}}{\mathrm{E_g}} = \frac{1240\ \mathrm{nm}}{\mathrm{E_g\ (in\ ev)}} \tag{II.1}$$

Where h is Planck’s constant, and c is the speed of light in a vacuum [5].

II.4.2 Optical properties of dielectric materials

Dielectric materials play a pivotal role in optical devices, being integral to most conventional optical components except for reflective surfaces. This stems from their exceptional ability to transmit light efficiently, enabling precise control over its properties. The interaction of light with dielectrics is analyzed using Maxwell's equations and the constitutive relations that link D to the E and B to the H [5].

At optical frequencies, we typically assume the relative permeability μ_r equals unity, simplifying the description of optical materials using the refractive index $n = \sqrt{\varepsilon}$. Despite the presence of dispersion and absorption phenomena, we often use a real value for n as a simplification, with Fresnel equations determining reflection and refraction behavior based on n and incidence angles [5].

MMs composed of metal-dielectric units exhibit strong dispersion, primarily attributed to their metallic components, particularly in the visible and near-infrared spectra. However, when examining the entire optical spectrum, the dispersion of transparent dielectrics becomes a significant factor that cannot be overlooked. Lattice vibrations and electron absorption determine the transparency range of these materials, necessitating careful selection of the dielectric in metamaterial design to avoid losses from electronic or photonic resonance [5].

The classical Helmholtz-Drude model describes the dielectric function ε(ω), which depends on resonance frequencies ω_j and damping constants γ_j. This model shows that transparent dielectrics exhibit absorption peaks at phonon resonance frequencies in the infrared and electron transition frequencies in the ultraviolet, while remaining transparent in the visible range due to the stability of the permittivity curve and weak absorption between resonance regions (as shown in Figure II.4).

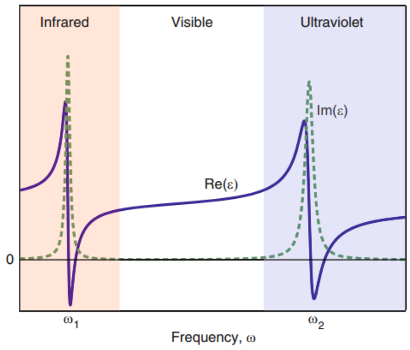

Figure II.4 The dielectric function ε(ω) for a typical dielectric material with the lattice resonance and electron transition resonance marked as ω_1 and ω_2, respectively [5].

The refractive index n remains connected to the dielectric function through the square root relation and is expressed as a complex number:

$$n(\omega) = n'(\omega) + in''(\omega) \; = \; \sqrt{\varepsilon(\omega)} \qquad \text{(II.2)}$$

For transparent dielectrics where n'' is very small, we use the Sellmeier approximation to describe dispersion without accounting for damping. In weakly absorbing media, the absorption coefficient α describes optical wave attenuation according to Beer's law [5].

II.4.3 Optical properties of metals

Traditionally, the use of metals in optics has been largely confined to mirrors and thin films. However, OMMs incorporate metals into their structure to achieve functional responses that exploit the significant contrast between the properties of metals and dielectrics. Metals exhibit high opacity and strong reflectivity at optical frequencies, with light being absorbed within a thin surface layer (skin depth) while most of it is reflected from their smooth surfaces. This behavior stems from free electrons that enable efficient photon absorption due to the continuity of the Fermi level [6].

Metals such as silver and aluminum demonstrate highly effective light reflection, whereas gold and copper display distinctive colors resulting from less efficient reflection of higher frequencies. These phenomena are analyzed through the dielectric functions of metals, as light-metal interaction depends on frequency-dependent permittivity determined by fundamental relations and the electron gas model describing free electron behavior in an electric field [5].

The EM response of metals is governed by the motion of free electrons within the crystalline structure, as described by the Drude model which assumes electron motion without a restoring force, leading to zero resonance frequency. When a time-varying electric field is applied, electron motion follows a differential equation yielding the frequency-dependent dielectric function:

$$\varepsilon(\omega) = 1 - \frac{{\omega_P}^2}{\omega^2 + i\Gamma\omega} = 1 - \frac{{\omega_P}^2}{\omega^2 + \Gamma^2} + i\frac{{\omega_P}^2\Gamma}{\omega(\omega^2 + \Gamma^2)} \tag{II.3}$$

Where ω_P represents the bulk plasma frequency that determines electron density oscillations, while Γ is the electron collision rate affecting optical absorption in metals. The parameter Γ relates to the mean free path of free electrons l and Fermi velocity v_F through:

$$\Gamma = v_F / l \tag{II.4}$$

The Drude model for the dielectric function in equation (II.3) requires refinement as it neglects the effect of bound electrons that become significant at higher frequencies such as those in the visible spectrum. Interband transitions, like the 5d to 6sp transition in gold, contribute to the dielectric function and can be represented using the Lorentz model, thereby complementing the description of free electrons in metals. Figure II.5 illustrates how interband transitions affect gold's dielectric function in the visible range, distorting it toward positive values and increasing absorption of blue and green light. Consequently, more yellow light is reflected, giving gold its characteristic color. Interband electron transitions continue influencing the dielectric function even at wavelengths much longer than the resonance wavelength, as shown in (Figure II.5). Therefore, at low frequencies, this effect can be approximated by a constant offset (1) to modify the Drude model for more accurate accounting of these transitions [5].

Noble metals exhibit negative permittivity at optical frequencies, causing most light to reflect at metal-dielectric interfaces. For silver's complex refractive index, the large imaginary component prevents deep light penetration, defining the skin depth at approximately 50 nanometers for optical frequencies. When metals are reduced to nanoscale dimensions, the damping factor in the Drude model changes due to size effects as the electron mean free path becomes constrained by the metal's physical boundaries. This increases the imaginary part of permittivity, affecting the optical properties of MMs and requiring consideration in designing nanoscale metal-dielectric structures [10].

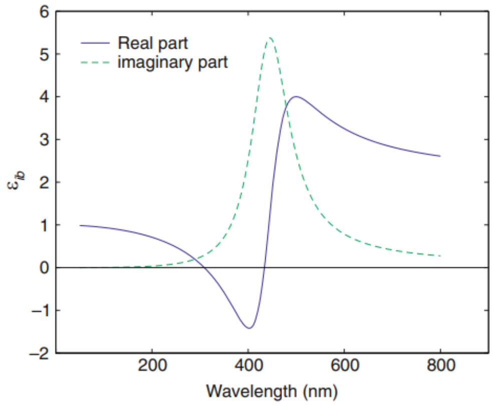

Figure II.5 Contribution of the interband transition to the permittivity of gold at visible frequencies ε_ib [5].

II.4.3.1 Plasmonics

Plasmonics provides profound insights into the interaction between metals and light at the nanoscale, serving as a cornerstone for developing advanced MMAs. When light strikes a metal surface, free electrons collectively oscillate, generating surface plasmon waves that concentrate at metal-dielectric interfaces (Figure II.6). This unique phenomenon results in significant local E field enhancement and extreme concentration of optical energy within subwavelength dimensions.

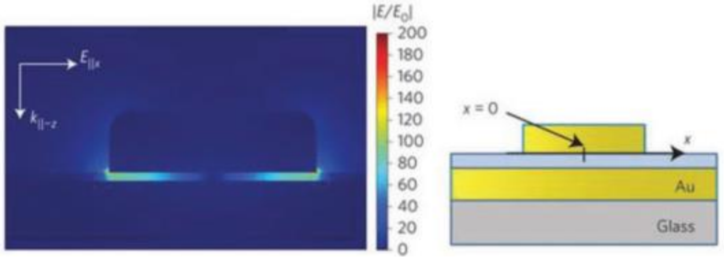

Figure II.6 EM field distribution within the nanostructure, showing strong plasmonic concentration areas at the edges of the nanodisk (left), and the geometric configuration of the system (right) [8].

Noble metals such as gold and silver exhibit exceptional plasmonic properties across visible and near-infrared spectra. These distinctive characteristics originate from the metals' negative permittivity, enabling researchers to overcome conventional diffraction limits and manipulate light at scales substantially smaller than its wavelength [10].

The technology finds diverse practical applications ranging from ultra-sensitive detection systems and precision photonic sensors to high-efficiency solar energy conversion. Current research is witnessing groundbreaking advancements in quantum plasmonics and dynamically tunable plasmonic systems [12].

II.4.4 Metal-insulator-metal (MIM) structures

MIM structures represent fundamental designs in the field of plasmonic MMs, offering an ideal solution for developing light absorbers in both optical and terahertz frequency ranges. These smart configurations consist of three integrated layers: a top layer containing an array of metallic nanostructures in various forms such as disks or rods, followed by a thin insulating layer, and finally a bottom metallic layer serving as a mirror, as illustrated in Figure II.7.

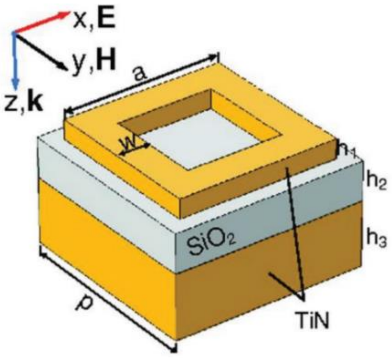

Figure II.7 Schematic representation of a unit cell of the three-layer MIM (TiN MMPA) [8].

The secret to these structures' effectiveness lies in the remarkable interaction between their components. When light strikes them, the metallic nanostructures in the top layer interact with the bottom metallic layer through the insulating layer, creating a unique resonant system. This system can effectively trap and convert light energy, thanks to the precise matching between its properties and the incident EM waves [12].

This technology boasts several exceptional characteristics that make it the optimal choice for numerous applications. The magnetic resonance generated between the metallic layers can achieve ideal light absorption conditions. The middle insulating layer plays a crucial role in adjusting resonance frequencies and absorption peak sharpness. Meanwhile, the bottom metallic layer reflects any escaping light waves, ensuring no portion of light energy is lost [10].

Moreover, these structures provide an ideal research platform for exploring advanced optical phenomena, such as surface plasmon effects and phase transitions in materials. This makes them indispensable tools for developing nanoscale systems requiring precise and customized optical responses, opening new horizons in the field of fine-tuned light control [12].

II.5 Applications

The origins of interest in electromagnetic wave absorption trace back to the World War II era, when militaries sought to conceal their ships and submarines from microwave radar detection. Today, these technologies have evolved to extend their applications across multiple domains serving modern needs [6].

II.5.1 Military and aeronautical

MMAs represent the cornerstone of modern military stealth technologies, effectively reducing the radar cross-section (RCS) of aircraft. These applications rely on advanced designs of polymer-based materials embedded with nanoparticles, enabling absorption of wide radar frequency ranges. Additionally, absorption characteristics can be adjusted according to operational requirements, whether for complete stealth purposes or for enhancing radar signatures in certain tactical scenarios [9].

II.5.2 Industrial and electronic

MMAs are widely used in creating high-performance anechoic chambers that employ pyramidal and conical configurations for efficient EM wave absorption [9]. They also play a critical role in solving electromagnetic interference (EMI) problems in precision electronic devices [11], improving system performance by reducing EM noise and unwanted coupling between adjacent electronic components, as well as creating EMI free zones as shown in Figure II.8.

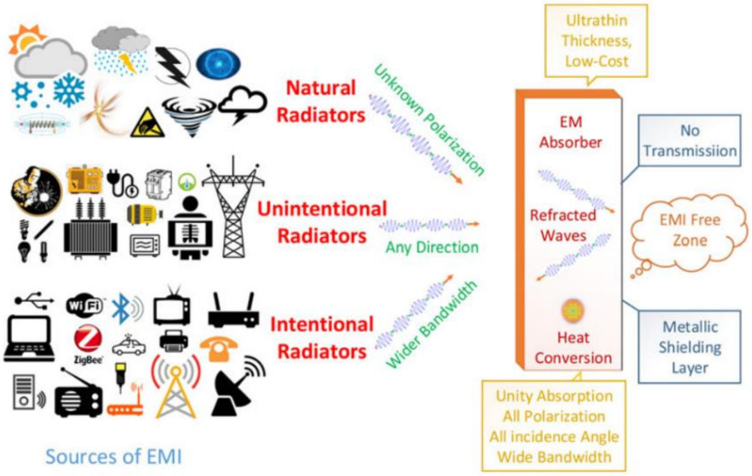

Figure II.8 Illustration of EM absorber [9].

II.5.3 Biochemical sensing

In the field of biochemical sensing, these materials leverage changes in resonance properties with variations in the surrounding medium, enabling them to achieve extraordinary sensitivity reaching 2513 nanometers per refractive index unit. Their effectiveness has been demonstrated in practical applications such as glucose and hydrogen detection using gold nanoplasmonics [6].

II.5.4 Energy harvesting

In the energy sector, these materials have emerged through advanced photodetection systems utilizing hot electrons that achieve over 90% efficiency in the visible spectrum. They have also contributed to innovative solutions for solar steam generation with thermal conversion efficiency up to 57% [6], along with thermophotovoltaic (TPV) systems that convert waste heat into electricity with very high efficiency in the system illustrated in Figure II.9.

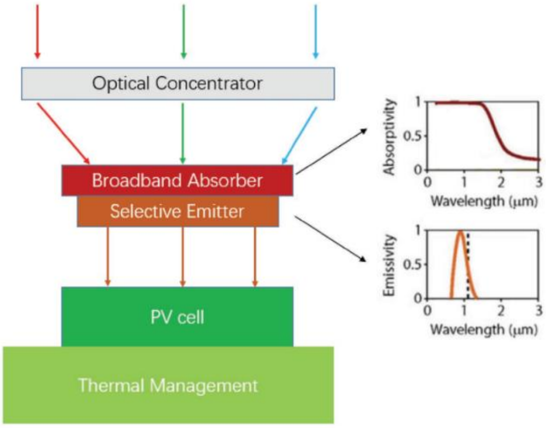

Figure II.9 Schematic of solar thermophotovoltaic (STPV) systems [8].

II.5.5 Imaging

In imaging technology, these materials have enabled the development of sophisticated systems including ultra-sensitive thermal imaging (37 picowatts per root hertz) and terahertz imaging with 5 mm resolution, as well as computational imaging techniques that operate efficiently under low illumination as minimal as 67 nanowatts [6].

II.5.6 Microwave and communications

MMAs contribute to the development of advanced communication components such as smart filters and high-efficiency signal amplifiers. In wireless communication systems, they enhance antenna performance by reducing unwanted side lobes, thereby improving data transmission efficiency. They are also used in wearable devices to reduce exposure to harmful EM radiation while maintaining communication quality [9].

II.6 Conclusion

This chapter concludes by presenting the theoretical foundations for understanding and designing MMs in the optical range. It has reviewed the historical development of these materials, emphasizing their unique ability to control EM response through precise structural design.

The chapter analyzed effective EM parameters such as permittivity and magnetic permeability, and their use in describing material behavior. It also examined the optical properties of metal-dielectric composites, highlighting the influence of microscopic structure and plasmonic effects in MIM systems.

Notably, the practical applications of these materials, particularly in solar energy harvesting which will be detailed in the following chapter (through numerical design and study of a metamaterial absorber), underscore their technological significance. MMAs open new horizons for developing high-efficiency devices with advanced spectral precision.

CHAPTER III METAMATERIAL ABSORBER FOR SOLAR ENERGY HARVESTING

III.1 Introduction

In recent years, MMAs have attracted increasing attention, thanks to the unique EM properties of MMs, such as negative permeability and negative permittivity. These features have expanded their range of applications in various fields such as solar energy harvesting, wireless communications, and sensors [14]. Modern applications require extremely high absorption rates and ultra-wide absorption bandwidths, so that the incident EM radiation is efficiently converted into other forms of energy. Solar energy is considered a promising option in this context, being a clean and renewable source that can contribute to solving global energy problems [15].

The performance of high-temperature solar thermal systems is often described in terms of the efficiency of converting solar energy into heat. Therefore, it is necessary to collect as much solar radiation as possible and reduce the loss caused by thermal emission in order to improve system efficiency. Hence, the selective absorber plays a crucial role in enhancing the thermal performance of solar energy systems [16]. In TPV cells, the absorber converts solar radiation into heat, which is re-emitted toward the PV cell within a selective range, allowing high-efficiency electricity generation [8]. To achieve this goal, the absorber must exhibit high absorption efficiency within the solar spectrum, low emissivity in the infrared range, and the ability to operate stably at high temperatures [17].

Since Landy and his colleagues proposed in 2008 the first perfect absorber capable of achieving 100% absorption at specific frequencies, research in this field has intensified [15]. However, narrowband absorbers are not sufficient to meet the practical needs of some applications, which has driven researchers to focus on developing broadband absorbers. Many studies have relied on multi-frequency resonance coupling to achieve strong absorption over wide bandwidths [18]. Additionally, the MIM structure has contributed to improving the absorption bandwidth, and most studies have focused on modifying the geometric dimensions and the shape of the top metal layer to enhance performance. For example, a triangular prism-shaped absorber demonstrated outstanding performance, with an average absorption of 97.85% in the range from 200-2980 nm [14].

In the field of solar energy absorption research, broadband MMAs are of great importance. There are many related studies, for example, Cheng and his colleagues proposed in 2022 a broadband solar MMA characterized by a variable longitudinal gradient [18]. Meanwhile, Zheng and his colleagues explored a cylindrical three-layer MIM structure that demonstrated an ultra-broadband solar absorber with an absorption rate exceeding 90% across the 280-3209 nm range, with an average absorption rate of 97.4% [19]. The four-layer disk arrangement of W/SiO_2 designed by Yi achieved full absorption with a rate exceeding 90% in the range of 420-1950 nm [16]. Wu and his colleagues also used the FDTD method to analyze a cylindrical three-layer MIM structure composed of Ti-Al_2O_3-Ti, resulting in an ultra-broadband solar absorber with an absorption rate exceeding 90% across the range of 244-3055 nm, and an average absorption rate of 95.8% [19].

Despite the progress made using stacked structures, there are still some challenges that limit the practical use of these absorbers, such as the need to improve absorption in the solar spectrum range and reduce thermal emission at high temperatures, which necessitates further design improvements [19]. Based on previously proposed structures by researchers, cylindrical, ring, and composite disk MIM configurations have shown promising performance in solar energy absorption [19]. Therefore, in this work, we propose a three-layer design composed of two concentric manganese (Mn) cylinders placed above a dielectric layer of Aluminum oxide (Al_2O_3), with an additional Mn layer acting as a reflective back mirror. This new simplified and specific composite structure enables ultra-wideband and high-performance absorption. We analyzed the properties of this absorber using the FDTD method, and studied the absorption mechanism at various frequencies through analysis of the EM field distribution and structural geometry. Compared to other absorbers, the proposed model possesses great potential in terms of efficiency and reliability, making it a promising candidate for the development of effective solar energy absorption technologies.

III.2 Theory

The FDTD method is used to solve Maxwell's equations in complex environments. It relies on direct computations in both time and space domains, offering accurate analysis of EM and optical phenomena [12]. It also allows for frequency-domain solutions through Fourier transforms, enabling the calculation of quantities such as the complex Poynting vector, as well as light reflection and transmission [20].

FDTD solves Maxwell’s curl equations in non-magnetic materials:

$$\frac{\partial \vec{D}}{\partial t} = \nabla \times \vec{H}, \text{ and } \vec{D}(\omega) = \varepsilon_0 \varepsilon_r(\omega) \vec{E}(\omega) \tag{III.1}$$

$$\frac{\partial \vec{H}}{\partial t} = -\frac{1}{\mu_0} \nabla \times \vec{E} \tag{III.2}$$

Where H, E, and D, are the magnetic, electric, and displacement fields respectively, while $\varepsilon_r(\omega)$ is the complex relative dielectric constant $\varepsilon_r(\omega) = n^2$ [20].

Assuming the structure is infinite in the z-direction and that the fields are independent of z, Maxwell's equations can be reduced into two independent sets, transverse electric (TE: E_x, E_y, H_z), and transverse magnetic (TM: H_x, H_y, E_z). In the TM case, the equations reduce to:

$$\frac{\partial D_z}{\partial t} = \frac{\partial H_y}{\partial x} - \frac{\partial H_x}{\partial y}, \text{ and } D_z(\omega) = \varepsilon_0 \varepsilon_r(\omega) E_z(\omega) \tag{III.3}$$

$$\frac{\partial H_x}{\partial t} = -\frac{1}{\mu_0}\frac{\partial E_z}{\partial y}, \text{ and } \frac{\partial H_y}{\partial t} = \frac{1}{\mu_0}\frac{\partial E_z}{\partial x} \tag{III.4}$$

These equations are solved on a discrete spatial and temporal grid known as the Yee cell [12], where each field component is calculated at a specific position within the cell. The software automatically interpolates the results to the origin of each grid point, simplifying the analysis for the user [20].

III.3 Proposed Structure

A schematic diagram of the unit cell and periodic array of the proposed MMA is illustrated in Figure III.1. At the top, an array of Mn double rings acts as a resonator [14]. An Al_2O_3 dielectric is used to separate the upper resonator from the bottom Mn layer, thus forming an MIM structure [16], and can induce EM coupling between them [14].

H_1 is the thickness of the Mn layer for the inner ring pattern with a width of D_1. H_2 is the thickness of the Mn layer for the outer ring pattern with a width of D_2. H_3 is the thickness of the separating Al_2O_3 dielectric layer, and H_4 is the thickness of the Mn substrate, and P is the periodicity of the absorber's structural unit, in order to achieve ultra-broadband perfect absorption and minimal absorber thickness, which is a fundamental constraint in achieving a perfect absorber [14], the geometric parameters of the proposed design were appropriately optimized, and the setting range for each parameter along with its optimal value was determined in Table III.1.

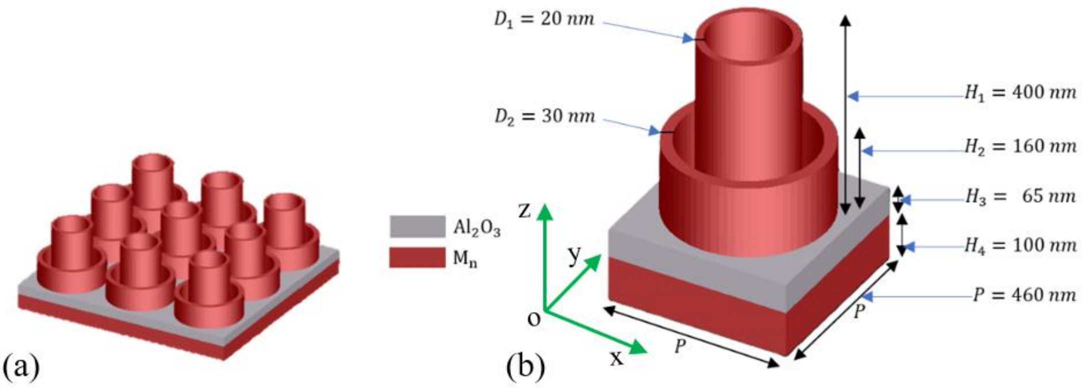

Figure III.1 a) Schematic representation of a periodic array of the proposed broadband metamaterial absorber, and b) schematic representation of a single absorber unit cell.

Mn was selected as the metallic layer due to the unique characteristics of its permittivity. The real part remains relatively stable across the visible spectrum, allowing good impedance matching with free space and enhancing EM field penetration into the structure. Additionally, the large imaginary part of its permittivity contributes to strong absorption. From a practical standpoint, Mn is also a cost-effective alternative to precious metals, which have been used in many broadband patterned absorbers. Al_2O_3 was also selected as a dielectric layer functioning as a spacer to excite plasmonic resonance [10], in addition to its excellent thermal resistance and low infrared absorption [18], which gives the model excellent selective performance [17].

Table III.1 List of geometrical parameters for the proposed absorber

Parameter	Decision space (nm)		Step (nm)	Optimum value (nm)
	From	To		
H_1	300	450	50	400
H_2	120	180	20	160
H_3	50	95	15	65
H_4	50	200	50	100
P	380	500	40	460
D_1	20	35	5	20
D_2	20	35	5	30

III.4 Results and discussion

We use the FDTD method to study the EM resonance and absorption performance of the proposed structure [22], and the absorptivity A is calculated using the equation A = 1 − R − T, where R represents reflectance and T transmittance [15]. It is worth noting that the thickness of the Mn substrate was chosen to be greater than the skin depth in the investigated frequency range, which ensures that the incident EM waves are unable to penetrate the absorber [21], resulting in transmittance (T = 0) [23], and thus the equation can be simplified to A = 1 − R. The average absorptivity of the absorber A_{aver} is calculated by integrating the absorption spectrum using the following formula [16]:

$$A_{aver} = \frac{\int_{\lambda_{min}}^{\lambda_{max}} A(\lambda)\cdot d\lambda}{\lambda_{max}-\lambda_{min}} \tag{III.5}$$

And to verify its practical use for solar energy, the absorption efficiency η_A of the absorber is calculated under the standard solar spectrum at AM 1.5 using the equation [21]:

$$\eta_A = \frac{\int_{\lambda_{min}}^{\lambda_{max}} A(\lambda)\cdot I_{AM1.5}(\lambda)\cdot d\lambda}{\int_{\lambda_{min}}^{\lambda_{max}} I_{AM1.5}(\lambda)\cdot d\lambda} \tag{III.6}$$

Where λ is the wavelength of incident light, A represents the absorptivity, $I_{AM1.5}$ denotes the solar spectra at AM 1.5, and λ_{min} and λ_{max} correspond to 300 nm and 4000 nm, respectively.

To explore the thermal emission characteristics of the solar absorber system, the thermal radiation efficiency η_E is defined by the following equation [22]:

$$\eta_E = \frac{\int_{\lambda_{min}}^{\lambda_{max}} \varepsilon(\omega)\cdot I_{BE}(\omega,T)\cdot d\omega}{\int_{\lambda_{min}}^{\lambda_{max}} I_{BE}(\omega,T)\cdot d\omega} \tag{III.7}$$

Where $I_{BE}(\omega, T)$ is the ideal blackbody spectral intensity at frequency ω and temperature T.

III.4.1 Evaluation of absorptive efficiency

The graphical illustrations shown in Figure III.2 provide a comprehensive representation of the absorber's characteristics over the studied wavelength range, and from it, across the entire wavelength range, it can be observed that the transmittance equals zero, while there is slight reflection around the range from 700-1200 nm, with a continuous gradual increase in reflectance after the wavelength of 2500 nm, which is a matter of interest for efficient selective solar absorbers [18]. As for the absorption curve, it provides strong evidence that the solar absorber we designed achieves an absorption rate exceeding 95% within a wide spectral range from 300-2799 nm, and exceeding 99% within a range it includes from 1100-2500 nm. It is worth noting that the proposed absorber achieves near-perfect absorption (about 100%) within a considerable range of 1020 nm ranging from 1200-2220 nm, and also at wavelengths 464 nm and 643 nm. Through the average absorption rate (A_{aver}), this exceptional performance is further enhanced, according to equation (III.5), where we can calculate that the average absorption reaches 98.80%, and within the range of 300-2500 nm, it reaches 98.24%. Accordingly, in general, these results indicate the great potential for achieving very high efficiency in solar energy harvesting.

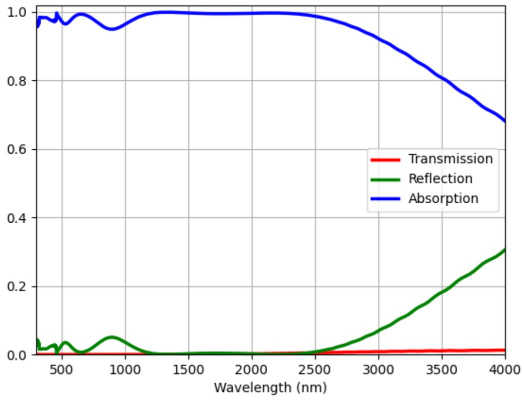

Figure III.2 Transmission, reflection and absorption spectra versus wavelengths.

The reason for the extremely high absorption of the proposed structure lies in the matching between its impedance and the impedance of free space. This matching can be verified theoretically if the scattering parameters (S-parameters) are known, where S_{11} and S_{21} are used to represent reflection and transmittance, respectively. And due to the presence of a thick bottom metal layer, S_{21} can be considered almost zero. Based on the S-parameters, the effective input impedance Z_{eff} can be calculated using equation (III.8) [14]. The simulation results in Figure III.3 illustrate the normalized impedance Z_{eff} of the absorber structure made of Mn, where it is observed that the real part of the impedance is close to 1, while the imaginary part is close to zero within the spectral range of 300-2500 nm, indicating a strong match between the absorber impedance and the free space impedance [17].

$$Z_{eff} = \sqrt{\frac{(1+S_{11})^2-{S_{21}}^2}{(1-S_{11})^2-{S_{21}}^2}} = \frac{1+S_{11}}{1-S_{11}} \tag{III.8}$$

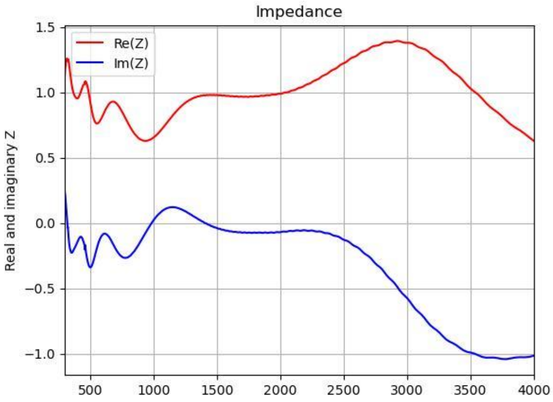

Figure III.3 Effective input impedance of the absorber design.

To provide a comprehensive explanation of the exceptional absorption capabilities of the proposed solar absorber, it can be easily concluded from equation (III.9) that, when the impedance of the absorber equals the impedance of free space, the reflectance R is zero [21]. And based on the previous equation A = 1 − R, it follows that the absorptance equals 1, which enables ultra-high absorption.

$$R = \left|\frac{Z-Z_0}{Z+Z_0}\right|^2 \tag{III.9}$$

Where R represents the reflectance of the absorber, Z_0 denotes the impedance of free space, Z signifies the impedance of the absorber.

III.4.2 Analysis of absorbed energy and radiated energy

To more closely match the actual light conditions on Earth [18], we obtained the solar radiation spectrum by placing the absorber at the optimum parameters in the AM1.5 spectrum [26], as illustrated in Figure III.4, where the black color indicates the AM1.5 solar radiation spectrum, the red color indicates the energy absorbed by the studied model, and the green color indicates the lost energy. By observing the spectral lines, it is evident that the solar energy absorption efficiency of the proposed solar absorber nearly reaches 100% of sunlight, and only a small amount of energy is lost, indicating that the absorber possesses ideal absorption and very high efficiency. This is further supported by using equation (III.6), where calculations reveal that over the range from 300 to 4000 nm, the average weighted absorption efficiency is 97.93%, with minimal energy loss of around 2.07%, once again proving that the designed absorber demonstrates a high capability of harvesting energy from solar radiation.

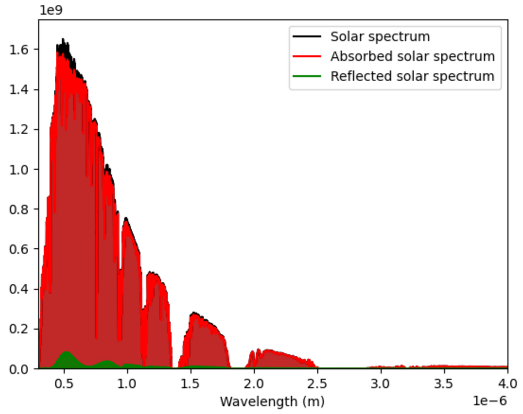

Figure III.4 Solar absorption spectrum and Analysis of energy loss and absorption.

In this solar absorber system, when compared to the ideal blackbody method, illustrated in Figure III.5, the thermal emitter exhibits nearly perfect emission intensity in the wavelength region up to 4000 nm at a temperature of 1000 Kelvin, and it possesses an excellent thermal radiation efficiency according to equation (III.7), reaching 97.76%, which is an impressive result.

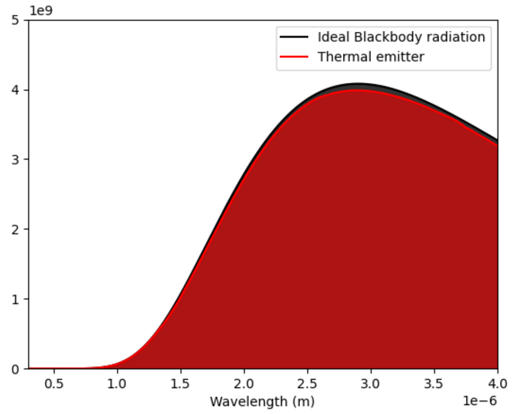

Figure III.5 Solar absorber energy emission diagram at 1000 K temperature.

In Table III.2, we present a comparison between the performance of the solar absorber we propose and some of the absorbers used in previous studies, with a focus on key performance criteria. The absorbers listed in the table demonstrated good absorption capabilities, but they failed to achieve an ideal balance between average absorption, bandwidth, and solar energy collection efficiency, as some overlooked factors such as thermal emission. In contrast, our proposed structure offers a comprehensive solution that combines a wide absorption range, high absorption rates, and high efficiency in managing thermal emission, making it suitable for applications in both solar energy collection and emission. Additionally, the simplicity of the design contributes to reducing production costs and facilitating the manufacturing process, which is closely linked to the materials used and the number of layers comprising the structure [14].

Table III.2 Comparison of Solar Absorbers from Previous Studies with the Proposed Structure

References	Structure thickness (nm)	Number of layers	Bandwidth (nm)	A %	$A_{aver}\%$	$\eta_A\%$	$\eta_E\%$
[14]	190	3	270	> 99	98.72	/	/
[15]	750	4	2570	95	98.10	97.90	/
[16]	1070	4	3354	90	98.30	98.86	94
[18]	1000	7	3720	90	94.10	94.80	/
[22]	1155	6	1869	90	96.56	95.89	92.83
Our work	565	3	1020	99.99	98.80	97.93	97.76
			2499	> 95	98.04		

III.4.3 Electromagnetic field intensity distribution

To understand the mechanisms behind the broadband and near-perfect absorption of the proposed metamaterial absorber, the field distributions in Figure III.6 show that the distributions were analysed at wavelengths of 480 nm, 550 nm, 1400 nm, and 2000 nm, where the figures (a) and (e) display the electric and magnetic fields at 480 nm respectively, while (b) and (f) highlight the distributions at 550 nm, (c) and (g) at 1400 nm, and finally (d) and (h) at 2000 nm.

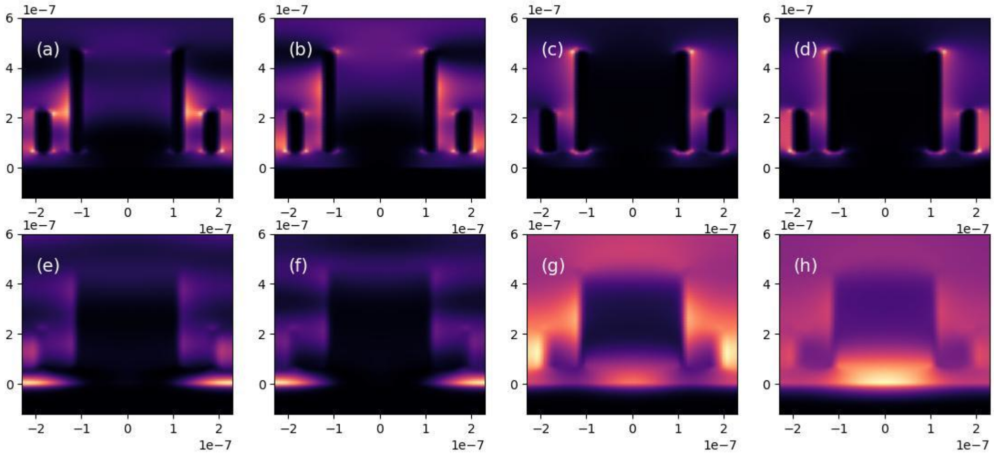

Figure III.6 Electric field distributions (a-d), and magnetic field distributions (e-h) of the proposed unit cell at different resonant wavelength peaks.

In figures (a) and (e) at 480 nm, a strong concentration of the electric field appears around the edges of the cylinders with a magnetic enhancement around the interfaces, indicating plasmonic and magnetic resonance that supports near-perfect absorption at 464 nm. As for (b) and (f) at 550 nm, the concentration continues around the edges with a slightly wider spread of both fields, enhancing high absorption in the visible range within the performance that exceeds 95% in

300-2790 nm. Regarding (c) and (g) at 1400 nm, the distribution is characterized by a more balanced spread and high intensity within the dielectric layer, reflecting a strong interaction that achieves near-complete absorption in the 1200-2220 nm range. Finally, in (d) and (h) at 2000 nm, the concentration remains strong around the cylinders with effective energy dissipation supporting high absorption within the same range. These distributions collectively highlight the mechanisms of light trapping and energy dissipation through plasmonic and magnetic resonances, leading to zero transmission, minimal reflection in 700-1200 nm, and absorption exceeding 95% across 300-2799 nm, with 99%-100% absorption in 1100-2500 nm, making the structure highly effective for solar energy harvesting.

III.4.4 Examination of microstructure

In order to illustrate the full benefits of the absorber structure that includes two Mn rings, we compared the absorption performance of several configurations: an absorber without any rings, an absorber with only the outer ring, and the proposed two-ring design absorber, while keeping all other factors unchanged, as shown in Figure III.7 a. As the absorption spectra in Figure III.7 b indicate, the presence of the outer ring alone clearly contributes to improving absorption, especially in the visible wavelength range. Furthermore, the use of two Mn rings leads to a significant enhancement in absorption efficiency across the entire studied spectrum.

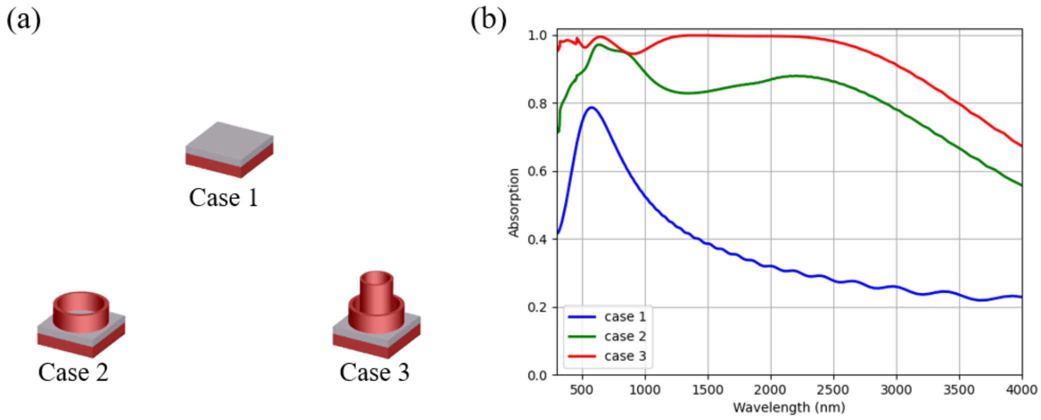

Figure III.7 a) A 3-D view of two different absorber configurations with the proposed design. b) Absorption spectrum for the two different absorber configurations with the proposed one.

This improvement can be explained by the dual-ring structure's ability to excite multiple resonance modes, such as surface plasmon resonance (SPR), cavity resonance (CR), and magnetic resonance (MR) [16].

III.5 Effects of material on the absorption property of the absorber

The effect of using different dielectric materials and metals on the absorption efficiency of the designed structure was studied. The dielectric material Al_2O_3 in the middle layer was replaced with several alternative dielectric materials such as Fe_2O_3, Si_3N_4, SiO_2, and HfO_2, while keeping the original structure dimensions and the used metal Mn unchanged. Figure III.8 illustrates the absorption spectra resulting from these modifications, where the results show a great similarity in the absorption performance among all tested dielectric materials, with SiO_2 and Al_2O_3 standing out as the two options offering better performance.

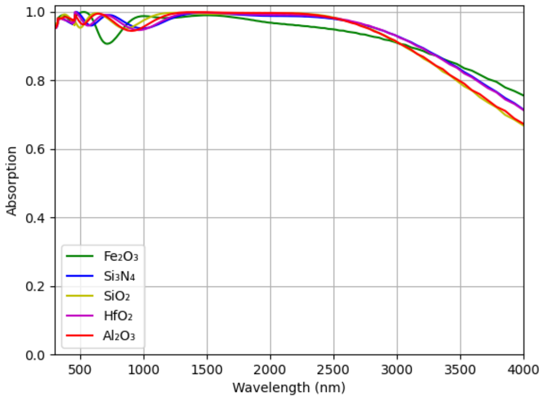

Figure III.8 Absorption spectra of the optimized structure with different dielectric materials.

As for the effect of replacing the metal, Mn in the top resonator layer and the bottom metallic plane was replaced with other metals such as nickel (Ni), titanium (Ti), and tungsten (W), while keeping the rest of the parameters unchanged. Figure III.9 shows the resulting absorption curves, where it is clear that most metals exhibit quite similar behavior within the range of 300 to 2000 nm, however, manganese still provides the best performance over the studied spectrum.

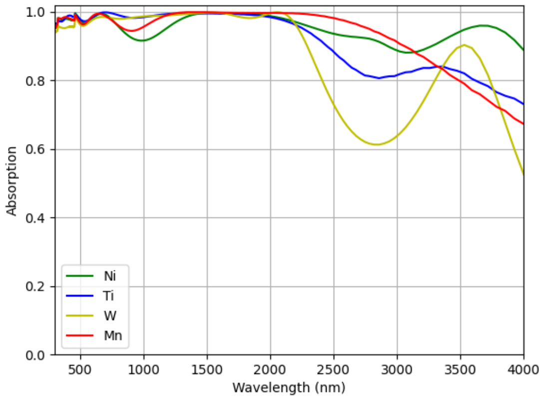

Figure III.9 Absorption spectra of the optimized structure with different metals.

This distinction is attributed to the good impedance matching between the Mn-based structure and the free space, making it the most suitable for enhancing the properties of the proposed absorber [14].

III.6 Adjustment of geometric parameters

The ideal absorber for practical use should have some margin for manufacturing errors [15]. Therefore, an analysis of the absorption spectra of the structure is conducted by systematically varying a specific parameter using the single-variable control method [21], where we investigate the absorption characteristics by individually altering each parameter while keeping the others constant.

III.6.1 Effect of top layer thickness on absorption performance

Initially, the investigation focuses on the effects of parameters associated with the manganese rings. Figure III.10 illustrates the impact of the inner ring thickness of the Mn patterned layer on the absorption characteristics, where it maintains the length of the optimal performance range while improving the performance ratio upon increasing, reaching the optimal value of 400 nm. Thus, increasing H_1 has little effect on stimulating resonance modes. Accordingly, the height of the inner Mn ring layer possesses a high geometric margin for manufacturing errors.

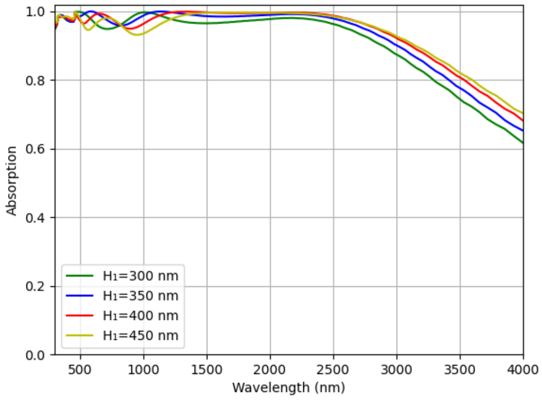

Figure III.10 Demonstrates the various absorption spectra of changing H_1.

Figure III.11 displays the effect of the outer Mn ring thickness on absorption performance. As H_2 increases, we observe a broadening in the solar energy absorption spectrum, with a relative improvement in the absorption rate within the near-infrared wavelength range. Therefore, the optimal value for H_2 is 160 nm, while maintaining a geometric margin for manufacturing errors.

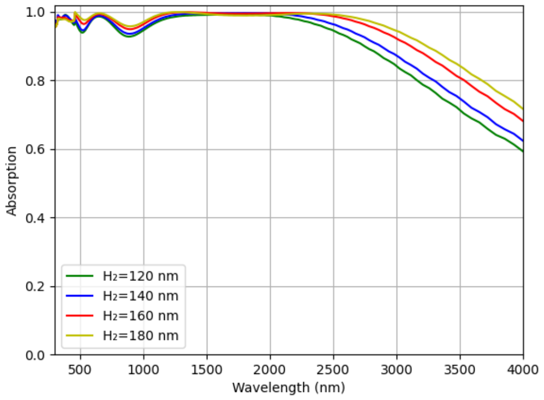

Figure III.11 Demonstrates the various absorption spectra of changing H_2.

III.6.2 Effect of dielectric and substrate thickness on absorption performance

The thickness of the dielectric layer Al_2O_3 varies from 50 to 95 nm. In Figure III.12, we observe that the absorptivity remains consistent in the regions achieving optimal absorption, and with increasing thickness, it shows improvement in the ultraviolet, visible, and near-infrared regions, indicating that a thickness of 65 nm is optimal for the dielectric layer H_3.

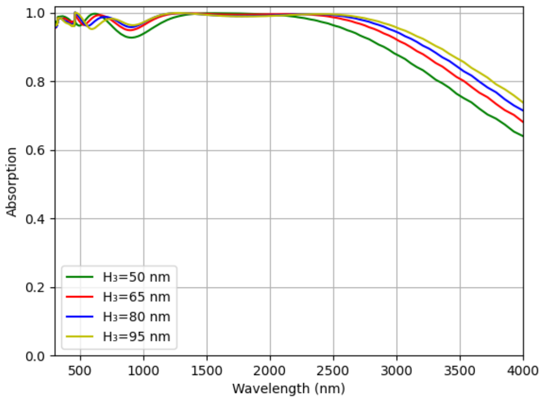

Figure III.12 Demonstrates the various absorption spectra of changing H_3.

These results in Figure III.13 indicate that the manganese layer, designated as H_4 and functioning as a substrate, exhibits a slight effect on the structure's absorption capacity when its thickness exceeds a certain limit, with the optimal value appearing at a thickness of 100 nm.

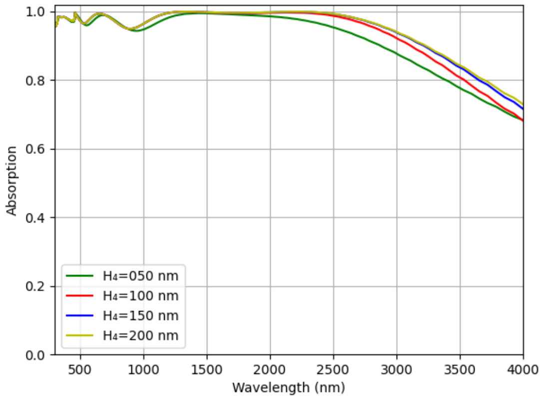

Figure III.13 Demonstrates the various absorption spectra of changing H_4.

III.6.3 Effect of structure period on absorption performance

Figure III.14 displays the effect of the absorber's period on absorption performance. An increase in the value of P beyond 2000 nm has an impact, thereby widening the bandwidth leading to absorptivity exceeding 95%, and subsequently, with continued increase, the bandwidth slightly decreases, resulting in an optimal P value of 460 nm, which achieves the best absorption.

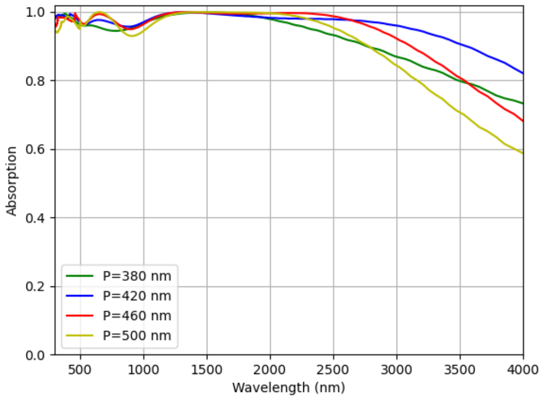

Figure III.14 Absorption spectra of the absorber for different values of the overall P.

III.6.4 Effect of ring width of inner and outer pattern on absorption performance

Figure III.15 displays the effect of the inner ring width of the Mn patterned layer on absorption performance. Good and consistent absorption performance is maintained while increasing the inner ring width D_1, with a slight change within the visible range, resulting in an optimal value at 20 nm.

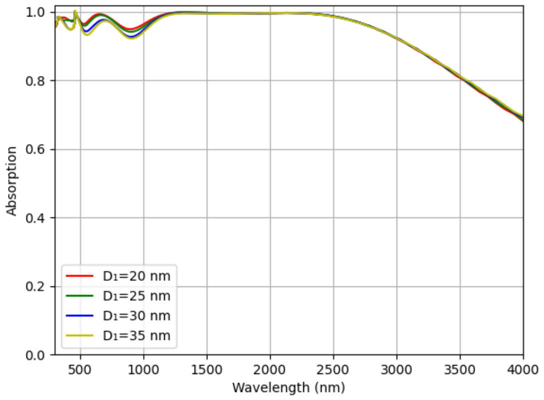

Figure III.15 Demonstrates the various absorption spectra of changing D_1.

As shown in Figure III.16, the effect of the outer ring width of the Mn patterned layer on absorption performance is evident. With an increase in the outer ring width D_2, the absorption performance remains consistent from 300 to 2000 nm, after which a slight change is observed, identifying 30 nm as the optimal value. Consequently, the widths of both the inner and outer rings can also tolerate a certain degree of manufacturing error.

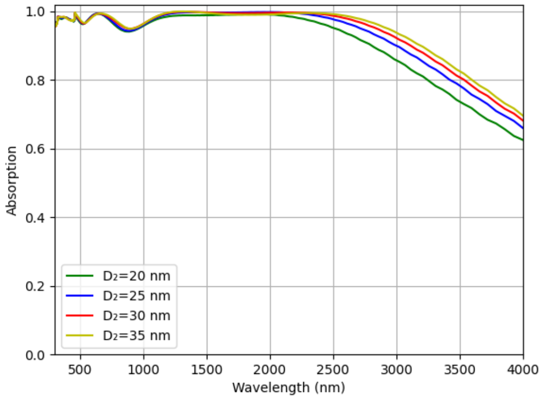

Figure III.16 Demonstrates the various absorption spectra of changing D_2.

Based on all this data, we find that even if some errors occur during manufacturing, the overall solar absorption efficiency remains high, indicating that the absorber possesses good manufacturing tolerance, even with slight deviations in structural parameters. This makes it suitable for practical applications requiring high precision, such as solar energy utilization in space stations and professional research experiments.

III.6.5 Conclusion

The newly developed broadband, high-efficiency solar absorber and thermal emitter has been designed for photovoltaic applications, utilizing a MIM (Mn_ Al_2O_3_Mn) structure crafted from cost-effective materials that exhibit strong resistance to high temperatures and oxidation. This design incorporates two concentric manganese rings with varying thicknesses and radii, meticulously optimized to enhance absorption performance. As a result, the structure demonstrates near-perfect absorption exceeding 99.99% across the wavelength range of 1200 to 2220 nm, over 99% within the 1100-2500 nm range, and more than 95% in the broader 300 to 2799 nm spectrum, with an average absorption rate reaching 98.04%. Under AM1.5 solar radiation conditions, the designed structure maintains an average absorption efficiency of 97.93% across the full spectrum from 300 to 4000 nm, with a minimal solar energy loss of less than 2.07%. Notably, when compared to an ideal blackbody, the absorber delivers exceptional thermal emission performance at 1000 Kelvin, boasting an impressive thermal radiation efficiency of 97.76%. This high performance is attributed to the synergistic effects of lattice resonance, surface plasmon resonance, Fabry-Pérot resonance, and both intra-structure and inter-structure plasmon coupling within the array. Furthermore, the design offers tolerance to minor geometric deviations, making it well-suited for practical manufacturing. These advantages highlight the proposed absorber’s potential as a promising candidate for next-generation solar energy systems and photovoltaic-thermal cells, while also providing clear reference value for developing electromagnetic metamaterial devices such as ideal absorbers, thermal emitters, and electromagnetic shielding.

CONCLUSIONS

This thesis has addressed the study of MMAs in the optical and terahertz domains, focusing on the design of a three-layer structure based on Mn cylinders and an Al_2O_3 dielectric layer, aiming to achieve highly efficient absorption for solar energy applications and photovoltaic-thermal cells. Through the three chapters, the theoretical foundations of electromagnetism were reviewed, starting with Maxwell's equations and concluding with the interaction of waves with materials. This was followed by an analysis of the unique properties of metamaterials and the operational mechanisms of their absorbers, culminating in the proposal of an innovative metal-insulator-metal structure that achieves near-perfect absorption exceeding 99.99% in the 1200 to 2220 nm range, with an average absorption efficiency of 98.04% across the broad solar spectrum.

This research encountered some challenges, such as the difficulty of optimizing the geometric design to ensure integration between lattice resonance, surface plasmon resonance, and Fabry-Pérot resonance, in addition to the need for precise simulations using the Finite-Difference Time-Domain method to ensure accuracy in analyzing the distribution of electromagnetic fields. It also required addressing challenges related to balancing the achievement of a broad absorption bandwidth with minimizing thermal losses at high temperatures. Despite these obstacles, the results demonstrated that the proposed design possesses manufacturing flexibility and high tolerance to minor geometric deviations, enhancing its practical feasibility.

Hence, it is recommended to continue research to develop diverse structures to improve performance in the terahertz ranges, with a focus on reducing manufacturing costs and enhancing thermal stability for high-temperature applications. It is also advised to study the impact of non-perpendicular incidence angles on absorption efficiency to expand the scope of applications. Finally, exploration of the integration of these absorbers with sensing technologies and thermal cooling systems is encouraged to support the development of advanced electromagnetic devices. This thesis seeks to provide a modest scientific contribution that paves the way for the development of innovative technologies in the fields of renewable energy and communications.

REFERENCES

[1] M. N. O. Sadiku, *Elements of Electromagnetics*, 7th ed. New York, NY, USA: Oxford University Press, 2018.

[2] S. W. Ellingson, *Electromagnetics*, vol. 1. Blacksburg, VA, USA: VT Publishing, 2018, doi: 10.21061/electromagnetics-vol-1.

[3] Y. H. Lee, *Introduction to Engineering Electromagnetics*, Heidelberg, Germany: Springer-Verlag, 2013, doi: 10.1007/978-3-642-36118-0.

[4] D. Fleisch, *A Student's Guide to Maxwell's Equations*. Cambridge, U.K.: Cambridge University Press, 2008.

[5] W. Cai and V. Shalaev, *Optical Metamaterials: Fundamentals and Applications*. New York, NY, USA: Springer, 2010.

[6] W. J. Padilla and K. Fan, *Metamaterial Electromagnetic Wave Absorbers*. San Rafael, CA, USA: Morgan & Claypool Publishers, 2022, doi: 10.2200/S01133ED1V01Y202109EMA004.

[7] M. A. Islam, M. J. Hasan, M. S. Chowdhury, J. Ghosh, and M. H. Mobarak, "Metamaterials for electromagnetic wave manipulation: Advancements and future prospects", *Nano-Structures & Nano-Objects*, vol. 41, p. 101424, Jan. 2025, doi: 10.1016/j.nanoso.2024.101424.

[8] P. Yu, L. V. Besteiro, J. Wu, et al., "Broadband Metamaterial Absorbers", *Advanced Optical Materials*, vol. 6, no. 1, p. 1800995, 2018, doi: 10.1002/adom.201800995.

[9] M. M. Tirkey and N. Gupta, "The quest for perfect electromagnetic absorber: a review", *International Journal of Microwave and Wireless Technologies*, vol. 11, pp. 151-167, 2019, doi: 10.1017/S1759078718001472.

[10] Z. Wang, Z. Liu, G. Duan, et al., "Ultrahigh broadband absorption in metamaterials with electric and magnetic polaritons enabled by multiple materials", *International Journal of Heat and Mass Transfer*, vol. 185, p. 122355, 2022, doi: 10.1016/j.ijheatmasstransfer.2021.122355.

[11] B.-X. Wang, X. Qin, G. Duan, G. Yang, W.-Q. Huang, and Z. Huang, "Dielectric-Based Metamaterials for Near-Perfect Light Absorption", *Advanced Functional Materials*, vol. 34, no. 18, p. 2402068, 2024, doi: 10.1002/adfm.202402068.

[12] K. L. Tsakmakidis, K. G. Baskourelos, and M. S. Wartak, *Metamaterials and Nanophotonics: Principles, Techniques and Applications*. Singapore: World Scientific Publishing, 2023, doi: 10.1142/13010.

[13] S. Kar, *Metamaterials and Metasurfaces: Basics and Trends. Bristol*, U.K.: IOP Publishing, 2023, doi: 10.1088/978-0-7503-5532-2.

[14] S. I. Sayed, K. R. Mahmoud, and R. I. Mubarak, "Design and optimization of broadband metamaterial absorber based on manganese for visible applications", *Scientific Reports*, vol. 13, p. 11937, 2023, doi: 10.1038/s41598-023-38263-x.

[15] S. Song, Y. Chen, S. Chen, J. Hou, and X. Huang, "An ultra-broadband high-performance solar energy perfect absorber from deep ultraviolet to mid-infrared", *Materials Today Communications*, vol. 39, p. 108712, 2024, doi: 10.1016/j.mtcomm.2024.108712.

[16] F. Wu, Y. Liu, L. Ling, et al., "Spectrally Selective Ultra-Broadband Solar Absorber Based on Pyramidal Structure", *Advanced Photonics Research*, vol. 4, no. 12, p. 2300305, 2023, doi: 10.1002/adpr.202300305.

[17] A. Shafique, M. A. Naveed, S. Ijaz, et al., "Highly efficient Vanadium Nitride based metasurface absorber/emitter for solar-thermophotovoltaic system", *Materials Today Communications*, vol. 34, p. 105416, 2023, doi: 10.1016/j.mtcomm.2023.105416.

[18] Y. Zhu, J. Cheng, Z. Yi, et al., "Spectrally selective solar absorber and thermal infrared suppression based on hollow cylindrical microstructures", *Optics Communications*, vol. 549, p. 129910, 2023, doi: 10.1016/j.optcom.2023.129910.

[19] Y. Xu, B. Wang, and J. Zhou, "Annular Ti-Al2O3-Ti triple-layer stacked composite microstructure solar absorber", *Applied Thermal Engineering*, vol. 263, p. 125449, 2025, doi: 10.1016/j.applthermaleng.2025.125449.

[20] Ansys, "Finite-Difference Time-Domain (FDTD) solver introduction", Ansys Optics Help Center. [Online]. Available: https://optics.ansys.com/hc/en-us/articles/360034914633-Finite-Difference-Time-Domain-FDTD-solver-introduction [Accessed: May 17, 2025].

[21] Q. Wang, X. Ju, Q. Lin, and J. Hu, "An ultra-broadband near-perfect solar absorber based on monolayer MoS2 with titanium ring-pillar arrays", *Optics Communications*, vol. 577, p. 131448, 2025, doi: 10.1016/j.optcom.2024.131448.

[22] Y. Zheng, P. Wu, H. Yang, et al., "High efficiency Titanium oxides and nitrides ultra-broadband solar energy absorber and thermal emitter from 200 nm to 2600 nm", *Optics & Laser Technology*, vol. 150, p. 108002, 2022, doi: 10.1016/j.optlastec.2022.108002.

[23] Z. Shen and J. Ni, "Multi-Resonant Full-Solar-Spectrum Perfect Metamaterial Absorber", *Nanomaterials*, vol. 14, no. 23, p. 1959, 2024, doi: 10.3390/nano14231959.

[24] P. Zeng, Y. Zhou, C. Zhang, et al., "Nanostructures/TiN layer/Al2O3 layer/TiN substrate configuration-based high-performance refractory metasurface solar absorber", *Scientific Reports*, vol. 14, p. 25827, 2024, doi: 10.1038/s41598-024-76118-1.

[25] X. Zhu and B. Wang, "Solar energy broadband capturing by metamaterial absorber based on titanium metal", *Journal of Chemical Physics*, vol. 160, no. 16, p. 164704, 2024, doi: 10.1063/5.0203486.

[26] Q. Liang, Y. Gu, J. Chen, et al., "Ultra-thin metamaterial solar selective absorber for enhanced photothermal conversion", *Optics Communications*, vol. 577, p. 131450, 2025, doi: 10.1016/j.optcom.2024.131450.

[27] C. Cen, X. Liu, Y. Lin, Z. Yi, and Q. Zeng, "Metamaterial absorber with ultra-broadband, ultra-high absorption, polarization independence and high-temperature resistance for solar thermal energy harvesting applications", *Optics Communications*, vol. 575, p. 131292, 2025, doi: 10.1016/j.optcom.2024.131292.

[28] J. Singh, A. Chopra, S. S. Pal, and S. Sarkar, "Nanoporous gold films as a perfect NIR-UV absorber", *Applied Surface Science*, vol. 685, p. 162005, 2025, doi: 10.1016/j.apsusc.2024.162005.

[29] X. Wang, Z. Liang, F. Yang, et al., "Chain-type multi-mode polarization-sensitive metamaterial absorber in infrared band", *Results in Physics*, vol. 68, p. 108105, 2025, doi: 10.1016/j.rinp.2024.108105.

[30] A. A. M. Rahman, M. T. Islam, M. Moniruzzaman, et al., "A highly absorptive ultra-wideband nanoscale metamaterial absorber for solar energy harvesting from ultraviolet to Infrared spectrum", *Ain Shams Engineering Journal*, vol. 16, p. 103229, 2025, doi: 10.1016/j.asej.2024.103229.